chemengineering

MDPI

Article

Fall and Rise: Disentangling Cycle Life Trends in Atmospheric Plasma-Synthesized FeOOH/PANI Composite for Conversion Anodes in Lithium-Ion Batteries

Evgenii V. Beletskii [1,*], Alexey I. Volkov [1], Ksenia A. Kharisova [1], Oleg V. Glumov [2], Maksim A. Kamarou [3], Daniil A. Lukyanov [1] and Oleg V. Levin [1,*]

[1] Institute of Chemistry, St. Petersburg State University, Universitetskaya Emb.7/9, 199034 St. Petersburg, Russia; a.i.volkov@spbu.ru (A.I.V.); st111412@student.spbu.ru (K.A.K.); lda93@yandex.ru (D.A.L.)

[2] Research Park, St. Petersburg State University, Universitetskaya Emb.7/9, 199034 St. Petersburg, Russia; o.glumov@spbu.ru

[3] Center "Plasma Physics", Belarusian State Technological University, 220006 Minsk, Belarus; makkom1995@gmail.com

* Correspondence: e.beletsky@spbu.ru (E.V.B.); o.levin@spbu.ru (O.V.L.); Tel.: +7-(812)-3636000 (O.V.L.) (ext. 9801)

Abstract: Various iron oxides have been proven to be promising anode materials for metal-ion batteries due to their natural abundance, high theoretical capacity, ease of preparation, and environmental friendliness. However, the synthesis of iron oxide-based composites requires complex approaches, especially when it comes to composites with intrinsically conductive polymers. In this work, we propose a one-step microplasma synthesis of polyaniline-coated urchin-like FeOOH nanoparticles (FeOOH/PANI) for applications as anodes in lithium-ion batteries. The material shows excellent electrochemical properties, providing an initial capacity of ca. 1600 $mA{\cdot}h{\cdot}g^{-1}$ at 0.05 $A{\cdot}g^{-1}$ and 900 $mA{\cdot}g^{-1}$ at 1.2 $A{\cdot}g^{-1}$. Further cycling led to a capacity decrease to 150 $mA{\cdot}h{\cdot}g^{-1}$ by the 60th cycle, followed by a recovery that maintained the capacity at 767 $mA{\cdot}h{\cdot}g^{-1}$ after 2000 cycles at 1.2 $A{\cdot}g^{-1}$ and restored the full initial capacity of 1600 $mA{\cdot}h{\cdot}g^{-1}$ at a low current density of 0.05 $A{\cdot}g^{-1}$. Electrochemical milling—the phenomenon we confirmed via a combination of physico-chemical and electrochemical techniques—caused the material to exhibit interesting behavior. The anodes also exhibited high performance in a full cell with NMC532, which provided an energy density of 224 $Wh{\cdot}kg^{-1}$, comparable to the reference cell with a graphite anode (264 $Wh{\cdot}kg^{-1}$).

Keywords: atmospheric plasma solution synthesis; lithium-ion batteries; FeOOH anode material; conversion metal oxide anodes; polyaniline

Citation: Beletskii, E.V.; Volkov, A.I.; Kharisova, K.A.; Glumov, O.V.; Kamarou, M.A.; Lukyanov, D.A.; Levin, O.V. Fall and Rise: Disentangling Cycle Life Trends in Atmospheric Plasma-Synthesized FeOOH/PANI Composite for Conversion Anodes in Lithium-Ion Batteries. *ChemEngineering* **2024**, *8*, 24. https://doi.org/10.3390/chemengineering8010024

Received: 15 November 2023
Revised: 18 January 2024
Accepted: 5 February 2024
Published: 10 February 2024

1. Introduction

Lithium-ion batteries (LIBs) have emerged as the most prominent energy storage devices, powering a wide range of applications, from smartwatches and laptops to electric vehicles and stationary energy storage systems [1]. Their success stems from high energy density, a long cycle life, and low self-discharge [2,3]. Nevertheless, there remains room for improvement, driving continuous research and development in all related aspects. Enhancing existing anode materials or developing new ones holds promise for increasing the specific capacity and energy density of LIBs [4,5].

The anode material with the most promising performance is lithium metal, with an extremely high theoretical specific capacity of 3860 $mA{\cdot}h{\cdot}g^{-1}$. However, its practical implementation is limited by safety issues caused by non-uniform lithium deposition and the growth of dendrites [6]. The latter is the object of many studies, but the proposed solutions are not yet mature [7]. Therefore, graphite anodes are conventionally used, yet their low theoretical specific capacity of 372 mA·h·g^{-1} limits their prospects in high-energy-density LIBs [8,9].

Many proposed solutions for novel LIB anodes are based on either single-phase (i.e., alloying) or multiple-phase conversion chemistry [9]. The latter group includes single or mixed transition metal oxides, including those of cobalt (II, (II,III)), nickel (II), copper (I), or iron (II, III, (II,III)) [5,10–13].

Such materials react with Li^+ in the electrolyte according to the reaction [5,14]:

$$M_aO_b + 2Li^+ + 2e^- \rightleftarrows aM + bLi_2O \quad (1)$$

Reaction Equation (1) results in the formation of sub 10 nm metal nanoparticles embedded into a lithium oxide matrix, as confirmed in the early 2000s by Debart et al. [15], and the capacities obtained from this reaction range from 650 mA·h·g^{-1} to 1000 mA·h·g^{-1} [9], depending on the specific material.

Various forms of iron(III) oxides and oxide-hydroxides are promising among other transition metal oxides as they have high theoretical capacity, are abundant in nature, are environmentally safe, and are sustainable [16–20]. Specifically, FeOOH is a semiconductor with a tunnel-type [21] or layered [22] structure, which favors lithium ion diffusion [23]. Its theoretical specific capacity is 905 mA·h·g^{-1} [24], and the average charge voltage of the electrode materials based on FeOOH, or its composites, is (1.5–2.0) V vs. Li/Li^+ [24–27]. The intermediate voltage made the initial studies regard FeOOH as a cathode material [28,29], though later the approach shifted to anodes due to the increased specific capacity of the material in the lower potential area.

Being a conversion electrode material, FeOOH recharges according to Equation (1), though the exact mechanism is disputed. The proposed mechanisms include the formation of metallic iron particles embedded in the Li_2O and LiOH matrix, followed by conversion between iron and FeO, rather than the initially present oxide-hydroxide [30]:

$$Fe^{III}OOH + 3Li^+ + 3e^- \rightarrow Fe^0 + Li_2O + LiOH \text{ (1st discharge)} \quad (2)$$

$$Fe^{II}O + 2Li^+ + 2e^- \rightleftarrows Fe^0 + Li_2O \text{ (the following cycles)} \quad (3)$$

After the initial discharge yielding 905 mA·h·g^{-1}, this mechanism suggests the consequent reversible cycling to provide the specific capacity of 603 mA·h·g^{-1} (referred to as the initial FeOOH content). However, the set of either peaks in cyclic voltammograms (CVs) or plateaus in galvanostatic charge–discharge (GCD) curves suggests a more complex recharging process than a simple two-electron reaction, such as this one [31]:

$$Fe^{III}OOH + Li^+ + e^- \rightleftarrows LiFe^{II}OOH \text{ (partially reversible) } (E \approx 1.70 \text{ V}) \quad (4)$$

$$LiFe^{II}OOH + xLi^+ + xe^- \rightleftarrows Li_{1+x}Fe^{II-x}OOH \text{ (partially reversible) } (E = 1.25 \text{ V}) \quad (5)$$

$$Li_{1+x}Fe^{II-x}OOH + (2-x)Li^+ + (2-x)e^- \rightleftarrows Fe^0 + Li_2O + LiOH \quad (6)$$
$$\text{(highly reversible) (E = 0.68 V)}$$

This set of reactions is additionally complicated by unspecified side reactions involving solid electrolyte interphase (SEI) and interfacial interactions near 0 V. The existence of Equation (4) is corroborated by earlier studies of FeOOH as a cathode material [32]. The drawback of such a description is that Equation (6) suggests a process involving three independent solid-state phases, which is an unlikely process regardless of the compounds involved. This might suggest that there is a mix of Equations (2)–(6) occurring in cells. Still, the transformation of Fe^{3+} into metallic iron should yield a specific capacity of 905 mA·h·g^{-1}. The extra capacity often reported in the literature might stem from the processes involving SEI [25–27], which warrants additional comments.

SEI has been extensively investigated for LIBs due to its existence, which is crucial for cell stability as it acts as a passivating medium on the electrode–electrolyte boundary during cycling [33]. Multiple studies have investigated the content of SEI and the factors affecting its functionality [34–38]. The processes occurring during battery cycling produce various compounds via electrolyte decomposition and polymerization and electrode–electrolyte interactions [33,39]. The commonly mentioned components of SEI are LiF [36], Li_xPF_y [40], $Li_xPO_yF_z$ [36,39], Li_2CO_3 [36], CH_3OLi, CH_3OCO_2Li [40], and RLi [41]. For the specific case of oxide-based conversion-type materials, such as FeOOH, there is a matter of reactions involving oxygen species that produce Li_2O [41,42] covered by an SEI with an electrochemically active polymer outer layer [42], which suffers reversible transformations during cycling [43,44]. The said electrochemical activity, which can even provide capacitive contribution [18,42], is mostly ascribed to an outer layer of SEI with an organic gel-like structure [45], as opposed to a denser internal layer composed primarily of Li_2O [44]. Thus, SEI is an essential and dynamically changing part of the cell, which is directly responsible for the electrodes’performance, and thus its nature and effects should be thoroughly considered.

While FeOOH can provide outstanding specific capacity values, there are certain challenges with the implementation of such a material. On its own, the material lacks electrical conductivity, especially because of the isolation of particles during cycling [32], partially caused by volumetric changes [25,46]. The problem exists for many conversion-type materials [10], and there are multiple approaches to eliminating it.

The first and oldest one is minimizing the particles’size [10], as nanosized particles provide more capacity and stability than their microsized counterparts [47,48]. For example, Ce-doped α-FeOOH nanorods (of ca. 70 nm to 80 nm diameter) provided up to 830 $mA \cdot h \cdot g^{-1}$ discharge capacity [24], while the capacity of β-FeOOH nanorods (of ca. 5 nm to 50 nm diameter) exceeded 1500 $mA \cdot h \cdot g^{-1}$ [49].

The second approach is the synthesis of the composites with carbon materials. Recent examples include F-doped FeOOH/graphene nanorods (~1207 $mA \cdot h \cdot g^{-1}$) [50], Si-doped FeOOH/graphene sheets (~1371 $mA \cdot h \cdot g^{-1}$) [25], or biomass-carbon-adhered β-FeOOH nanorods (~1450 $mA \cdot h \cdot g^{-1}$) [51]. This approach has proven useful due to the increased surface area and presence of a conductive carbon-based matrix, though graphene is also a popular choice for other anode materials [52].

The third approach is the design of the composites with conducting polymers (CPs), which may eliminate the problems related to a lack of conductivity and mechanical strain caused by volumetric changes during cycling. The properties of CPs, such as intrinsic electronic conductivity and mechanical flexibility, as well as their own charge storage capacity [53], make this approach feasible. The use of CPs in electrode materials for energy storage devices has proven useful in enhancing their specific capacity, cyclic stability, rate capability, and plastic features [54–56], and they were shown to be beneficial for composite electrode materials based on both typical intercalation compounds [57] and transition metal chalcogenides [58,59]. Examples of successful implementation of FeOOH/CPs include FeOOH@PEDOT (1335 $mA \cdot h \cdot g^{-1}$) [26] and β-FeOOH@PEDOT (726 $mA \cdot h \cdot g^{-1}$) [60]. FeOOH/PPy composites have been successfully used in supercapacitors [61,62]. To the best of our knowledge, the composites of PANI with FeOOH have not been used in LIB anodes, though early studies attempted to use such composites as a cathode material [63], and FeOOH/PANI-based materials were found to be useful in microbial fuel cells [64] and wastewater treatment [65]. The composites of a related compound, Fe_2O_3, have also been studied as a material for energy storage devices; e.g., Fe_2O_3/PANI can be used in supercapacitors [66] or LIBs [67,68].

Plasma-assisted synthesis performed via plasma–liquid interactions has proven useful for obtaining nanomaterials with various compositions and morphologies [69–72]. Atmospheric plasma synthesis was performed to obtain FeOOH nanoparticles for catalysis [73], and by introducing graphite in the reaction mixture, we have synthesized FeOOH/graphite nanocomposites for anode materials in LIBs [74]. Various modifications of plasma-assisted synthesis were also suitable for CPs, including PANI, for various applications [75–77]. Obtaining a composite such as FeOOH/PANI in a similar way is thus a promising avenue to explore, as CPs tend to increase the stability and rate capability of conversion-type electrode materials [26,78].

In this work, we applied a novel method for the synthesis of FeOOH/PANI composites, which has not been used before, and described the promising use of this material in lithium-ion batteries, which is also the first time that this specific material has been used in such an application. The anode materials based on this composite provide outstanding specific capacity values exceeding 1600 mA·h·g^{-1} at 0.05 A·g^{-1} and retain 767 mA·h·g^{-1} by the 2000th cycle at 1.2 A·g^{-1}, exceeding that of pristine FeOOH by 120%. PANI serves as a conducting agent in the composite and prevents material dissolution. The improved electrochemical properties of the material can be attributed to the electrochemical milling effect, which reorganizes the material, and the formation of an electrochemically active SEI, thereby further enhancing the cycling performance.

2. Materials and Methods

2.1. Material Preparation

Plasma solution electrolysis was carried out using a custom glass cell setup (Wuhan Corrtest Instrument Corp., Wuhan, China), illustrated in Figure S1 Supplementary Materials**)**. An IWT-NY-Nylon Membrane (0.22 μm pores, I.W. Tremont Co., Hawthorne, NJ, USA) separated the anodic and cathodic cell spaces, preventing electrolyte mixing (aqueous solution of 50 mM $FeSO_4$ and 1 mM aniline sulfate). Electrode separation was essential to isolating the reaction products at the plasma–liquid interface. The anode, situated 2 mm from the electrolyte surface and placed normally in relation to it, comprised a stainless-steel capillary tube (inner diameter of 80 μm, length of 4 cm, Varian, Inc., Palo Alto, CA), with argon gas flowing at 50 cm^3·min^{-1}. The negative electrode was a 3 × 4 cm^2 stainless-steel mesh. A microplasma, sustained by a positively biased DC power supply, was initiated at the argon tube outlet. Throughout the experiments, the microplasma interacted with the 1 mm^2 electrolyte surface. The discharge current was around 0.9 ± 0.1 mA at 2 kV. Electrolysis continued for 3 h with constant stirring. The resulting FeOOH/PANI composite was precipitated, washed, and vacuum-dried at 90 °C for 24 h.

2.2. Electrode Preparation

The acquired powders were mixed with carbon black “Super P” (Timcal Inc., Willebroek, Belgium) and PVDF binder (Solef® 6010, Solvay, Brussels, Belgium) in a weight ratio of 70:20:10 using N-methylpyrrolidone (Vecton, St. Petersburg, Russia) to form a dense slurry that was applied onto a Cu foil (MTI, China) via doctor-blading with a 100 μm gap, resulting in an active material loading of approximately ~1 mg·cm^{-2}.

For full cell tests, the cathode material was prepared via a similar procedure by mixing NMC532 with carbon black and PVDF in an 80:10:10 weight ratio, followed by applying it onto Al foil (MTI, China) with a gap of 200 μm, producing coatings with ~4 mg·cm^{-2} active material loading.

All electrodes were vacuum dried at 90 °C for 24 h and subsequently roll-pressed before the cutting and assembly processes.

2.3. Electrochemical Measurements

Cell assembly took place in an argon-filled glove box (Vilitek, Moscow, Russia). CR2032 cells were assembled with the composite serving as the cathode and lithium metal foil (0.6 mm thick, Aldrich, St. Louis, MO USA) as the anode. Celgard 2320 (Celgard, Inc., Charlotte, NC, USA) separators were placed between electrodes, and the cells were filled with 1 M $LiPF_6$ in ethylene carbonate/diethyl carbonate (1/1 v/v ratio) electrolytes.

The electrochemical performance of the materials in CR2032 cells was further studied at room temperature. Cyclic voltammograms (CVs) were recorded using a Biologic VMP-

3 electrochemical workstation (Biologic, France) at scan rates ranging from 0.1 $mV \cdot s^{-1}$ to 5 $mV \cdot s^{-1}$ within a potential range of (0.01–2.85) V (vs. Li/Li^+). Galvanostatic discharge/charge measurements were carried out on a BTS 4000 battery test system (Neware, Hong Kong, China) at various current rates within the (0.01–2.85) V range. Electrochemical impedance spectra (EIS) were recorded using a Biologic VMP-3 potentiostat over a frequency range from 10 kHz to 10 mHz.

To investigate the evolution of materials throughout their cycle life, electrochemical impedance spectra of representative cells and data from the potentiostatic intermittent titration technique were collected at potential levels of 2.85, 2.5, 2.0, 1.5, 1.0, 0.5, and 0.01 V after 5, 60, 150, 500, 1200, and 2000 cycles. Following this, the cells were disassembled in an argon-filled glove box. Cathodes were thoroughly rinsed with diethyl carbonate and subsequently dried for 24 h. SEM/EDX, ATR-FTIR, and XPS analyses were performed on the samples after 5, 60, 150, 500, 1200, and 2000 recharging cycles.

The full battery was prepared as follows: After cycling 2000 cycles, coin cells were dissembled in an Ar-filled glovebox and the FeOOH/PANI electrode was extracted and washed with an electrolyte solution. Further, a full battery with a cathode based on NMC532 was assembled in CR2032. Celgard 2320 (Celgard, Inc., Charlotte, NC, USA) was used as a separator and 1 M $LiPF_6$ in ethylene carbonate/diethyl carbonate (1/1 volume ratio) as an electrolyte. Gravimetric energy density was calculated based on the total weight of the electrode material. The battery was cycled at a C/2 current density for 50 cycles.

2.4. Additional Material Characterization

SEM imaging as well as EDX mapping of both of the obtained composites and the electrodes were conducted using the Zeiss Merlin microscope (Carl Zeiss Microscopy GmbH, Jena, Germany). The cycled electrodes were studied with Fourier-transform infrared spectroscopy with an attenuated total reflection module (ATR-FTIR) on a Thermo Nicolet 8700 spectrometer (Thermo Fisher Scientific, Waltham, MA, USA). Details of XPS measurements of both synthesized powders and cycled electrodes are provided in the Supporting Information.

For conductivity measurements, tablets with a diameter of 4.5 mm and a thickness of approximately 0.6 mm were prepared by compressing the powders and placing them between silver electrodes. The conductivity of FeOOH/PANI powders was investigated with electrochemical impedance spectroscopy using an Autolab PGSTAT 302N potentiostat/galvanostat. Measurements were carried out in the 100 Hz to 1 MHz range at (20–125) °C in a dry N_2 atmosphere with a residual oxygen pressure of less than 10^{-3} atm.

3. Results and Discussion

3.1. Characterization of FeOOH/PANI

SEM images in Figure 1a,b illustrate the urchin-like structure of the FeOOH/PANI particles obtained. The diameter of the particles is ca. (600–900) nm on average, and the particles form agglomerates of up to 1200 nm (Figure S2a). In addition, we can see that the needles themselves are quite heterogeneous, often sticky, and covered with a layer of PANI, with an average needle thickness of ca. (20–50) nm (Figure S2b). The synthesis of FeOOH in similar conditions without the addition of aniline sulfate produces particles with more homogeneous and thin needles up to 10 nm in diameter (Figure S4a,b). Their shape and thickness changed upon the addition of aniline sulfate (Figure S4c,d) to resemble those in FeOOH/PANI images. Plasma electrochemical synthesis of PANI from aniline sulfate solution produces spherical agglomerates of up to 20 nm in diameter. A similar composite has been obtained by oxidative in situ polymerization of aniline in the presence of iron oxide [79]. In addition, the model of FeOOH large (ca. 500 nm) particle agglomeration into an urchin-like structure during chemical oxidation of iron sulfate describes [80] the fast process of iron sulfate oxidation as the one that leads to a *kinetically* favorable structure of spherical particles with a smooth surface, whereas the slow process leads to a *thermodynamically* favorable structure with an urchin-like morphology through the needle-forming stage. These facts suggest that the oxidation of Fe^{2+} with the formation of FeOOH occurs with simultaneous polymerization of aniline at the contact site of the electric discharge with the solution, due to which PANI coats FeOOH needles, which then agglomerate into an urchin-like structure.

The "needles" of the urchin-like particles exhibit a fibrous heterogeneous structure with a diameter of (30–50) nm, leading to a decreased degree of material crystallization and higher amorphization. EDX spectra in Figure S4e confirm the composition of the material, which consists primarily of iron and oxygen, with the presence of sulfur from SO_4^{2-}. The element ratios obtained from EDX spectra are 2.86 for O/Fe and 4.42 for Fe/S. The oxygen content in the samples exceeds the expected 2:1 value for FeOOH, as it is likely that a compound with a structure of schwertmannite—a sulfate-containing mineral—was obtained, as the synthesis conditions were the same as reported earlier [74]. The obtained XRD pattern (Figure S3) shows that the closest match for this material is indeed schwertmannite (PDF 47-1775) [81], though the obtained powder is X-ray amorphous, complicating the exact determination of the phase.

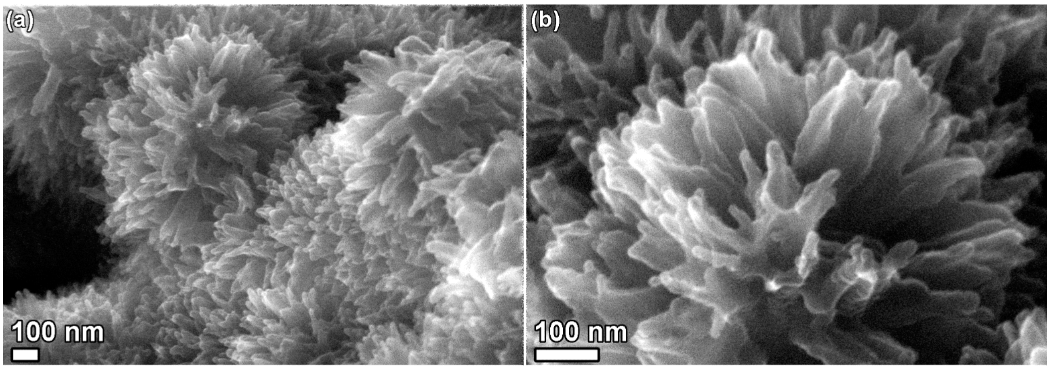

Figure 1. (**a**,**b**) FeOOH/PANI SEM images at different magnification.

There is a Fe $2p_{3/2}$ peak with Gupta-Sen multiplet components in the Fe 2p XPS spectrum in Figure 2a [82]. Their intensities and the binding energy (BE) of the low-energy component (710.4 eV) align with the Fe 2p spectra of FeOOH [83–85]. The O 1s peak (Figure 2b) is approximated by three components, with two attributed to FeOOH [83,86,87] and one high-energy component to SO_4^{2-} species [81,82]. The S 2p level spectrum (Figure 2c) agrees with this, exhibiting only one chemical component attributed to highly oxidized sulfur (i.e., SO_4) [88,89]. The N 1s spectrum from PANI reveals an imine nitrogen at the 398.7 eV peak, a protonated nitrogen at 400.4 eV (benzenoid amine (-NH-)), and an oxidized amine at 400.8 eV [90–92]. The doping level, determined by the ratio of N^+ to the total nitrogen content, was approximately 13% [93], and the total nitrogen content in the sample was ca. 2.5 at %.

The specific electrical conductivity of the FeOOH/PANI composite is ca. 8.12×10^{-5} $S{\cdot}cm^{-1}$, surpassing the conductivity of FeOOH (~10^{-10} $S{\cdot}cm^{-1}$ to 2.41×10^{-10} $S{\cdot}cm^{-1}$) by five orders of magnitude, as reported in our previous work [74] and in the literature [94]. The addition of PANI to FeOOH increased the electrical conductivity of the composite because a 13% PANI doping level corresponds to a highly conductive form of the polymer [91,95,96]. The PANI doping level was evaluated by a close inspection of the N 1s envelopes to determine the positively charged nitrogen (N^+) contribution to the total nitrogen content [91]. FeOOH/PANI showed (Figure S4f) two orders of magnitude increases in electrical conductivity upon the increase in the temperature from 18 °C to 130 °C. Notably, the $\ln\sigma$–$1000/T$ curve is not linear, as expected for semiconducting materials, but FeOOH [97] and PANI [98] are. For FeOOH, the conductivity change upon heating is associated with the dehydration of OH^- pairs in the surface layers, resulting in the formation of mono-charged oxygen vacancies that provide Fe^{3+} with electrons that reduce it to Fe^{2+} at $T < 140$ °C [97]. In PANI, the linear conductivity growth is limited to dehydration and the de-doping temperature [99], after which the decrease replaces the growth. In the case of PANI doped with SO_4^{2-} this temperature is 229 °C. Fe^{3+} in FeOOH can additionally oxidize PANI at lower temperatures, producing Fe^{2+} in the surface FeOOH layers and, as a result, causing an earlier change in the lnσ–$1/T$ curve. Such behavior of the material can be very favorable when discharged by powerful modes accompanied by heat release, which would decrease the internal resistance of the cell.

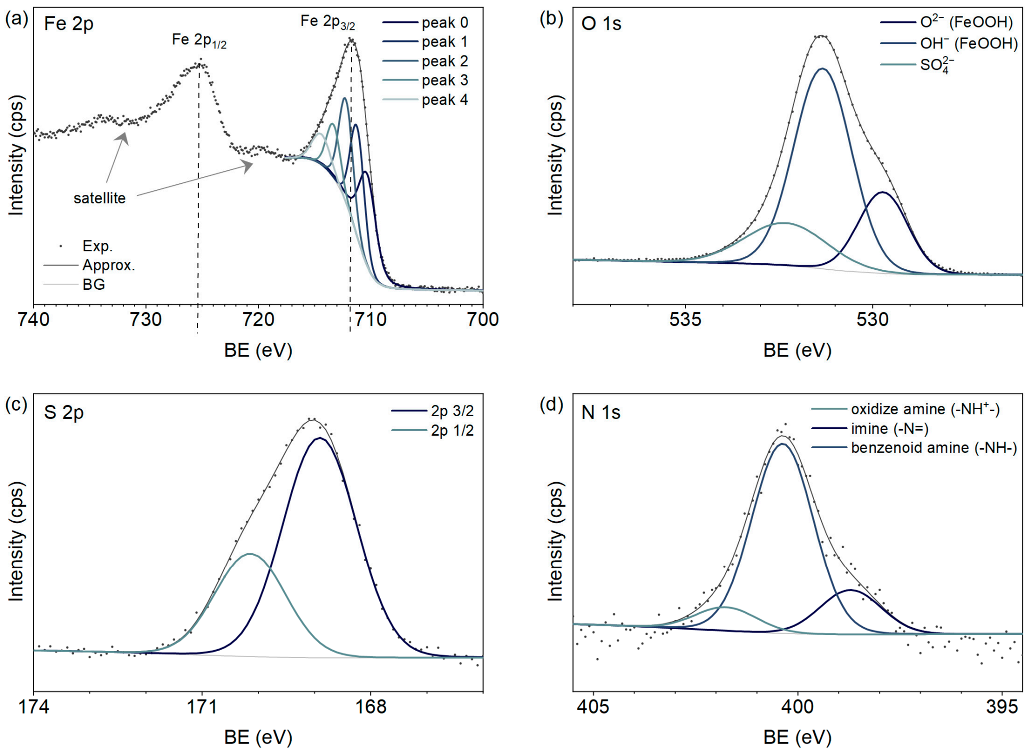

Figure 2. XPS spectra of FeOOH/PANI: (**a**) Fe 2p; (**b**) O 1s; (**c**) S 2p; (**d**) N 1s.

3.2. Electrochemical Performance

The FeOOH/PANI electrode exhibits significant irreversibility during the first recharging cycle, similar to other negative electrode materials [100,101]. In the initial discharge, it delivers 1595 mA·h·g^{-1}, but this drops to 1082 mA·h·g^{-1} in the subsequent charge (Figure 3a), resulting in a Coulombic efficiency of 68%. The notably high value in the first discharge, surpassing the theoretical capacity, can be attributed to the concurrent processes of the initial conversion of FeOOH and the formation of the SEI layer [25–27]. With further cycling at a current of 0.05 A·g^{-1}, the capacity drops to 527 mA·h·g^{-1} by the fifth cycle. Increasing the current density further reduces the material capacity, reaching about 17 mA·h·g^{-1} at 10 A·g^{-1}. Overall, the C-rate capacity retention of the FeOOH/PANI composite is comparable to that of the FeOOH composite with graphite [74]. Following C-rate capability testing with currents up to 10 A·g^{-1}, the FeOOH/PANI electrode retains a residual capacity of 320 mA·h·g^{-1}.

In our previous work [74], the capacities of FeOOH and its graphite composite increased during long-term cycle life tests at 1.2 A·g^{-1}. After 2000 cycles, the capacity of pure FeOOH was 349 mA·h·g^{-1}. We added a conductive material—graphite—to improve the long-term cycling behavior and increase the capacity of the composite FeOOH/graphite material, which became 543 mA·h·g^{-1} by the 2000th cycle.

Similarly, we subjected FeOOH/PANI to prolonged cycling by up to 2000 cycles to verify the long-term capacity increase. At 1.2 A·g^{-1} (Figure 3b), the initial capacity of

FeOOH/PANI is 936 mA·h·g^{-1}. The large value aligns with those commonly observed for conversion-type materials at the beginning of cycling. Then, as the large particles of active materials become coated with a non-conducting SEI layer, a significant capacity fade occurs (142 mA·h·g^{-1} at the 70th cycle). Following that, the capacity starts to increase, reaching 767 mA·h·g^{-1} by the 2000th cycle. Thus, a clear improvement in the electrochemical performance of composites with conductive components occurs. Pure FeOOH showed 349 mA·h·g^{-1}; composite with graphite, 543 mA·h·g^{-1}, and with PANI, 767 mA·h·g^{-1}. It also shows that coating FeOOH with PANI gives it a 41% edge over FeOOH-coated graphite in terms of electrochemical performance.

A similar increase in capacity of conversion-type anode materials has been demonstrated for cobalt and iron oxides [42,43,102,103], and it can be attributed to two mechanisms: the formation of an electroactive gel polymer layer—an integral part of SEI [42,43,102,103]—and the electrochemical milling [102,104], a phenomenon observed in metal oxide anodes. The combination of these two effects results in the opposite effects of SEI during cycling. At the beginning of cycling, there is a gradual decrease in the size of the active material particles, which leads to the formation of new SEI on their surface, and hence the capacity decreases. In addition, both inorganic lithium salts, which constitute the outer surface of the SEI, and electrochemically active oligomers, which constitute the inner surface of the SEI directly adjacent to the surface of the metal particles, are formed. The oligomers are formed by the catalytic reduction of carbonate solvents on the surface of iron particles. These oligomers are reversibly oxidized and reduced during the charge–discharge process discussed in detail in [42,43,102,103].

The initial cathodic scan of the FeOOH/PANI composite in the CVs (Figure 3d) reveals a broad peak at ~1.75 V, corresponding to Equation (4), followed by distinct peaks at 1.12 V, 0.54 V, and ~0 V. These peaks are attributed to the lithium insertion Equations (5) and (6), and the subsequent reduction of electrolyte components with SEI formation, respectively [31,105,106]. The subsequent anodic scan shows a well-defined peak at 1.12 V, characteristic of this material [31,105,106], followed by a broad peak at 1.50 V, corresponding to the conversion Equation (6). Almost indistinguishable shoulders at 2.00 V and 2.50 V may be ascribed to Equations (4) and (5), respectively. In subsequent cycles, only a broad cathodic peak at 0.54 V related to the reduction of Fe-based non-stoichiometric oxides persists. The CV cycling reveals a decrease in peak intensities over 20 cycles, consistent with cycling behavior and C-rates, likely linked to the pulverization of FeOOH/PANI and SEI formation.

At the current density of 0.05 A·g^{-1} (Figure 3c), the first discharge curve of the FeOOH/PANI electrode exhibits three plateaus at 1.89 V, 1.41 V, and 0.82 V, representing the initial reduction of the material into the metallic form of iron in Li_2O clusters, similar to conversion-type anodes like Co_3O_4 [107], and the formation of the SEI. By the third cycle, the charge curve retains only two plateaus, corresponding to two redox processes in alignment with the CV data.

To estimate the changes after 2000 cycles at 1.2 A·g^{-1}, we conducted C-rate and cyclic voltammetry tests. The C-rate testing results show (Figure 3a,c) a significant capacity increase overall. At 0.05 A·g^{-1}, its value is ca. 1600 mA·h·g^{-1} in the first discharge, stabilizing after five cycles and remaining at the same level after other C-rates. The power density of the material also improves, as is suggested by the results of higher C-rates studies. At 10 A·g^{-1}, the capacity in the 50th cycle is only 7.77 mA·h·g^{-1}, as opposed to 182 mA·h·g^{-1} after 2000 cycles. The transformation of the charge storage mechanism is associated with the evolution of the charge–discharge curves towards a more capacitor-like profile under prolonged cycling or at high current density. This shift reflects a transition from the dominant FeOOH conversion reaction to the faradaic charging of a newly formed gel polymer layer on the electrode surface.

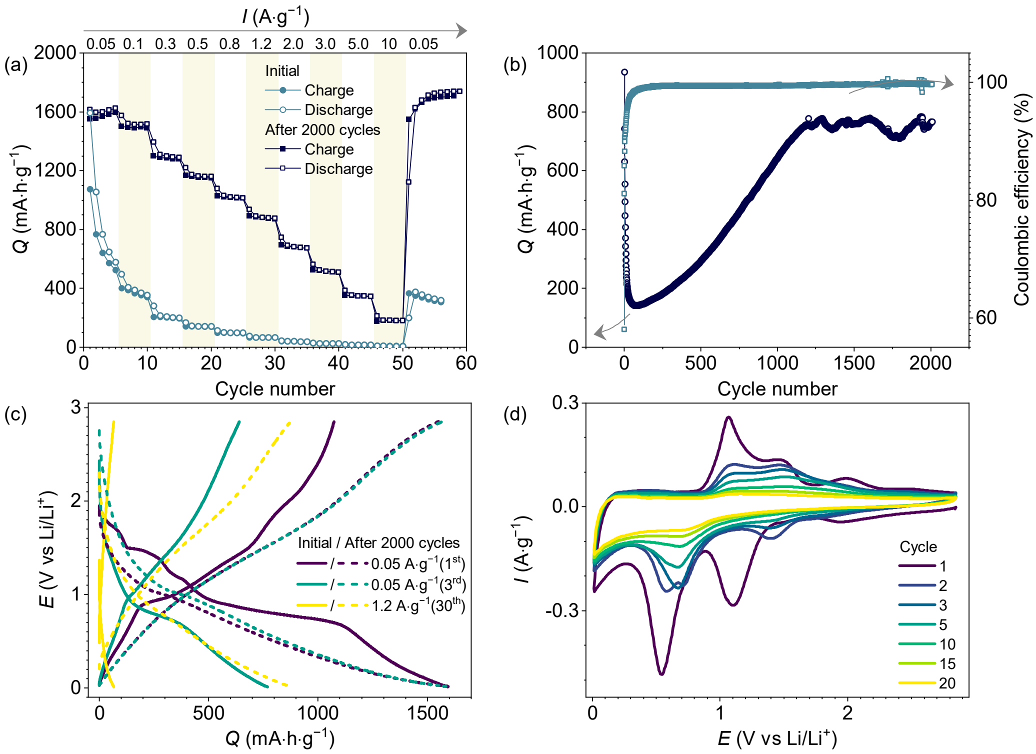

Figure 3. Electrochemical performance of FeOOH/PANI electrode: (**a**) C-rate capability; (**b**) cycling stability at I = 1.2 $A{\cdot}g^{-1}$; (**c**) charge/discharge curves during C-rate capability; (**d**) cyclic voltammograms at 0.1 $mV{\cdot}s^{-1}$.

This matches the observations for CVs similarly obtained after 2000 cycles (Figure 4) at 0.1 $mV{\cdot}s^{-1}$, which show peaks shift from 1.12 V to 1.59 V and from 0.68 V to 0.92 V for anodic and cathodic scans, respectively, and peak intensities increase fivefold. These observations suggest that specific surface areas and contact between particles increase in the FeOOH/PANI material after long-term cycling and stable SEI formation [74].

Upon increasing the scan rate to (0.2–5) $mV{\cdot}s^{-1}$, the distinct peaks in the cyclic voltammogram (CV) (Figure 4a) gradually fade, giving rise to a quasi-rectangular capacitive response. The FeOOH/PANI electrode demonstrates predominantly pseudocapacitive behavior across a range of scan rates, exhibiting a subtle anodic peak around 1.4 V without well-defined cathodic peaks. After 2000 cycles, a significant increase in peak intensities is observed, and the CV shape at higher scan rates becomes more rectangular, suggesting a potential enhancement in specific surface area (Figure 4b).

As is shown in the insets of Figure 4a,b, the slope (b values of two redox peaks, see Equation (7)) before and after 2000 cycles reaches ~0.75. This suggests that the electrochemical reaction processes are controlled by both pseudocapacitive (or surface-located) and diffusion mechanisms. To evaluate the reaction kinetics and separate diffusion and pseudocapacitive contributions to the total current, CV curves from Figure 4a,b were analyzed. The total current i can be separated into capacitive $i_c = k_1 v$ and diffusion-limited processes $i_d = k_2 v^{1/2}$, where v is the scan rate, according to (7) [108–110]:

$$i = a{\cdot}v^b = k_1{\cdot}v + k_2{\cdot}v^{1/2} \quad (7)$$

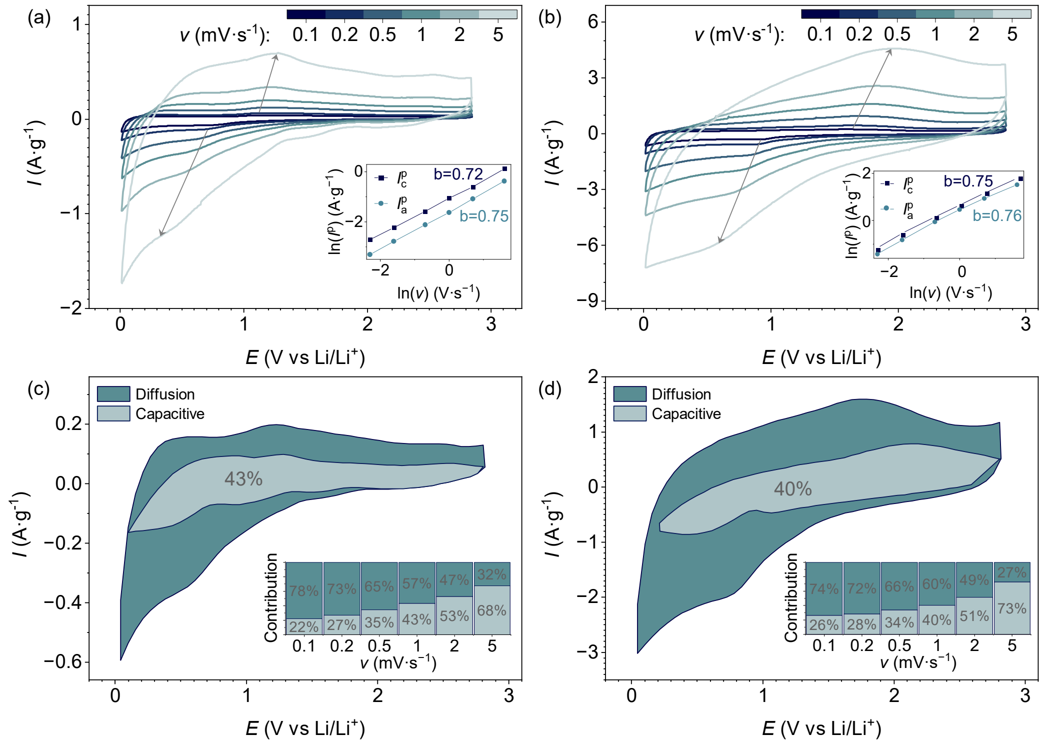

Figure 4. FeOOH/PANI after 20 cycles: (**a**) CVs at various scan rates; inset shows ln(I_{peak}) vs. ln(v) plot; (**c**) pseudocapacitance contribution to total capacity at 1 mV·s^{-1}, inset shows contribution ratios of capacitive and diffusion-controlled currents at various scan rates. FeOOH/PANI after 2000 cycles: (**b**) CVs at various scan rates; inset shows ln(I_{peak}) vs. ln(v) plot; (**d**) pseudocapacitance contribution to total capacity at 1 mV·s^{-1}, inset shows contribution ratios of capacitive and diffusion-controlled currents at various scan rates.

At a scan rate of 1 mV·s^{-1} (Figure 4c,d), 57% and 60% of the total charge are stored through diffusion-controlled processes after 20 and 2000 cycles, respectively. As the scan rate increases, charge storage via capacitive processes rises to 68% and 73%, respectively. Therefore, at low scan rates, Li^+ ion diffusion limits the overall electrochemical reactions, while pseudocapacitance becomes the dominant charge/discharge mechanism with increasing scan rates (insets of Figure 4c,d). The high capacitive contribution is attributed to the large surface area of nanosized particles and their high electronic interconnectivity [26].

The FeOOH/PANI material shows a similar pseudocapacitance contribution regardless of the number of cycles. High pseudocapacitive currents both after 20 and 2000 cycles are likely due to PANI components of the composite being readily available for charge transfer facilitation regardless ofvthe FeOOH surface area. The latter increases the total specific current values, yet the ratio of diffusion and pseudocapacitive currents remains the same.

The characteristics of FeOOH/PANI presented in this study are consistent with the most recent literature, as summarized in Table 1. Due to the inherent variability in the values obtained for conversion materials during the initial cycles, more precise data for each cycle can be found in the cited works. It is important to note that *reduction* capacities have been reported in certain instances. While this is a crucial property for *positive* electrode (*cathode*) materials, it is essential to report *oxidation* capacity when evaluating prospective *negative* electrode (*anode*) materials used as *cathodes* against a Li *anode*. Our findings highlight the remarkable stability of the materials, demonstrating a sustained increase in capacity over approximately 1900 cycles following the initial restructuring.

Table 1. Comparison of performance of FeOOH-based and related materials in LIBs anodes.

Material	Specific Capacity, $mA\cdot h\cdot g^{-1}$ (Current Density)	Stability, Capacity Retention (Cycles)	Ref.
Fe_3O_4/graphene sheets	600 (0.1 $A\cdot g^{-1}$)	80% (100)	[11]
Functionalized porous carbon/β-FeOOH	737.1 (0.2 $A\cdot g^{-1}$)	122% (350)	[18]
Fe_2O_3 nanotubes	950 (0.05 $A\cdot g^{-1}$)	98% (30)	[111]
β-FeOOH	275 (0.1 $mA\cdot cm^{-2}$)	n/a	[21]
Carbon cloth/β-FeOOH nanorod arrays	2840 (1 $A\cdot g^{-1}$)	90% (150)	[23]
Ce-doped α-FeOOH nanorods	1260 (0.1 $A\cdot g^{-1}$)	86% (800)	[24]
Si-doped FeOOH nanorods@graphene sheets	1370.5 (0.1 $A\cdot g^{-1}$)	>100% (200)	[25]
Graphene/FeOOH	1100 (0.1 $A\cdot g^{-1}$)	n/a	[46]
β-FeOOH/rGO	781.5 (0.1 $A\cdot g^{-1}$)	n/a ~90% (100)	[112]
FeOOH@PEDOT	1341 (0.5 $A\cdot g^{-1}$)	113.6% (270)	[26]
Biomass carbon/β-FeOOH	1450 (0.2C)	64% (100)	[51]
FeOOH/GO	1437 (0.1 $A\cdot g^{-1}$)	93.35% (100)	[113]
FeOOH/SWNT	905 (0.1 $A\cdot g^{-1}$)	~95% (180)	[105]
β-FeOOH	~1400 (0.2 $A\cdot g^{-1}$)	~43% (1 to 600) ~210% (70 to 600)	[31]
Mn-doped α-FeOOH	1147 (0.5 $A\cdot g^{-1}$)	184% (90 to 300)	[106]
Fe_2O_3/PANI	1200 (0.5 $A\cdot g^{-1}$)	62.5% (100)	[67]
h-Fe_3O_4@PANI	1350 (0.1 $A\cdot g^{-1}$)	81% (50)	[79]
Fe_2O_3/PANI	1055 (0.2C)	61% (150)	[68]
α-Fe_2O_3	1119 (1C)	176% (600)	[102]
FeOOH	640 (0.05 $A\cdot g^{-1}$) and 356 (1.2 $A\cdot g^{-1}$)	245% from 15^{0t}h to 200^{0t}h cycle (356 $mA\cdot h\cdot g^{-1}$ end value)	Previous work [74]
FeOOH/Gr	840 (0.05 $A\cdot g^{-1}$) and 543 (1.2 $A\cdot g^{-1}$)	206% from 6^{0t}h to 200^{0t}h cycle (543 $mA\cdot h\cdot g^{-1}$ end value)	Previous work [74]
FeOOH/PANI	1600 (0.05 $A\cdot g^{-1}$) 767 (1.2 $A\cdot g^{-1}$)	540% from 7^{0t}h to 200^{0t}h cycle (767 $mA\cdot h\cdot g^{-1}$ end value)	This work

3.3. Full Battery

After cycling the coin cells at 1.2 $A\cdot g^{-1}$ for 2000 cycles, we disassembled them in an Ar-filled glove box and replaced lithium foil with NMC532 cathode. The voltage curves (Figure 5a) and the trends of the capacity and coulombic efficiency (Figure 5b) of the NMC532//FeOOH/PANI full cell referred to the cathode mass show that it provides a stable response at the constant current rate of C/2 (1C = 140 $mA\cdot h\cdot g^{-1}$), reaching 125 $mA\cdot h\cdot g_{cathode}^{-1}$ at the start of the tests and 116 $mA\cdot h\cdot g_{cathode}^{-1}$ (826 $mA\cdot h\cdot g_{anode}^{-1}$) in the following cycles, and its coulombic efficiency approaches 97% (Figure 5b). The respective voltage profile in the first cycle shows lower coulombic efficiency, which we ascribe to the side processes, i.e., electrolyte decomposition and cathode electrolyte interphase film formation [114,115], which, in addition, cause structural reorganization of the material. The decrease in capacity over the first five cycles is a feature of the NMC532 electrode and can be attributed to the ongoing structural reorganization of the material. The same material in a half-cell with a lithium anode shows a similar capacity profile over five initial cycles [116]. Furthermore, the voltage profiles at the 2nd, 5th, 10th, 25th, and 50th cycles show a monotonous sloped signal centered at ca. 2.5 V, reflecting the conversion of FeOOH in the FeOOH/PANI anode and the simultaneous Li^+ deintercalation of the NMC532 cathode that reversibly occur during the cycling of the full cell.

Considering the discharge profile for the 25th cycle shown in Figure 5a and the cell composition, we estimate that the practical gravimetric energy density of the NMC532//FeOOH/PANI cell approaches 224 Wh·kg^{-1}, which we compared to a traditional assembly with a graphite anode (NMC532//Graphite). Gravimetric energy density of this cell was calculated in the same way as for NMC532//FeOOH/PANI, and its value was 264 Wh·kg^{-1}. The NMC532//FeOOH/PANI cell demonstrates a gravimetric energy density comparable to the traditional NMC532//Graphite. This, combined with the low cost and high cyclic stability of FeOOH/PANI, makes it a promising alternative to commercial anode materials.

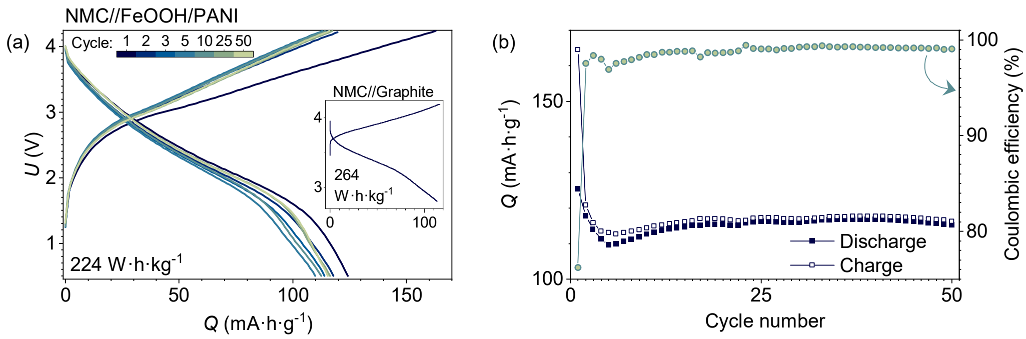

Figure 5. NMC532//FeOOH/PANI full cell performance within the (0.5–4.20) V range at C/2 referred to the NMC532 cathode mass (1 C = 140 mA·g^{-1}) in terms of (**a**) selected voltage profiles, *inset*: charge–discharge curve of the NMC532//Graphite full cell at a C/2 rate; (**b**) trends of specific capacity and coulombic efficiency. Electrolyte: 1 M $LiPF_6$ in EC/DEC (1:1, v/v).

A comparison of the full cell energy density with the literature data for various anode systems (Figure 6) shows that the characteristics of the full cell are comparable with other oxide-based conversion anodes (e.g., $(Co_{0.2}Cu_{0.2}Mg_{0.2}Ni_{0.2}Zn_{0.2})O$ [117]) on the one hand, and are at the lower end of the silicon and carbon-based anode series on the other hand. However, the complicated composition and specific reagents make the synthesis of such compounds labor-intensive, which would ultimately affect the economic attractiveness of the product.

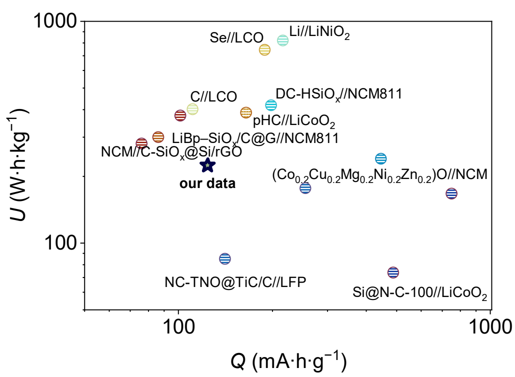

Figure 6. Comparison of NMC532//FeOOH/PANI full cell with other anodes in development: Si@N-C-100//$LiCoO_2$ [118], NC-TNO@TiC/C//LFP [119], NMC811//DC-$HSiO_x$ [120], Li//$LiNiO_2$ [121],

LCO-Se [122], pHC/$LiCoO_2$ [123], LiBp-SiO_x/C@G//NCM811 [124], NCM//C-SiO_x@Si/rGO [125], and ($Co_{0.2}Cu_{0.2}Mg_{0.2}Ni_{0.2}Zn_{0.2}$)O [117].

3.4. Post Cycled Electrodes

To elucidate the mechanism of the FeOOH/PANI-base electrode capacity increases during cycling, we obtained impedance spectra at 5, 60, 150, 500, 1200, and 2000 cycles and characterized electrodes after these cycles by ATR-FTIR, XPS, SEM/EDX methods. Also, diffusion coefficients were calculated from PITT measurements with the Cottrell approach according to [126] at 2.85, 2.5, 2.0, 1.5, 1.0, 0.5, and 0.01 V for the 5th, 60th, 150th, 500th, 1200th, and 2000th cycles.

The impedance spectra of the FeOOH electrode recorded at the charged and discharged states of the half-cells after 5, 60, 150, 500, 1200, and 2000 discharge/charge cycles are presented in Figure 6. Nyquist plots show two distinct semicircles in the discharged state (Figure 7a) and one semicircle in he charged state (Figure 7b). In the discharged, state the first semicircle can be attributed to the passivation film on the surface, or SEI, and the second semicircle refers to the charge transfer resistance of the Li^+ absorption/desorption process at the interface [127,128]. In the charged state, a single semicircle is attributed solely to the SEI, and the charge transfer resistance is negligible. The significant decrease in charge transfer resistance is similar to the case of the FeOOH/graphite composite we reported previously [74].

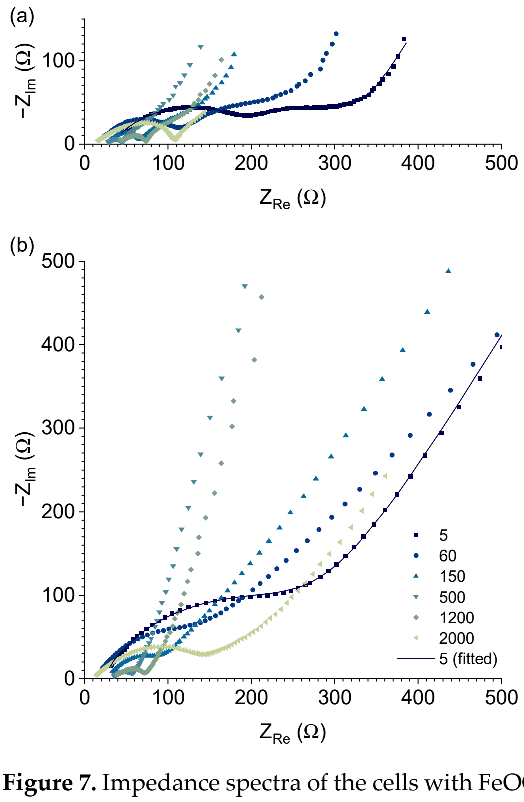

Figure 7. Impedance spectra of the cells with FeOOH electrodes at intermediate points during long-term cycling at OCV (**a**) after discharge and (**b**) after charge.

It is clear from Table 2 that the half-cell in the charged state demonstrates a monotonic increase in Q_1 (i.e., SEI capacitance), which indicates an increase in the SEI coverage of the active material/electrolyte interface due to FeOOH electrochemical milling, which we illustrated in [74], and is characteristic of metal-oxide anode materials [104].

The R_s value in the charged state, which refers to the electrolyte resistance, does not seem to follow any trend and remains in the ca. (12–38) Ω range.

Since using a capacitor in an equivalent circuit did not yield an adequate fitting curve, a constant-phase element (CPE) was used in a pair with the R_1 resistor. The CPE element produced the Q_1 capacitance value and the a parameter, which is a CPE exponent defining the behavior of the CPE element depending on its value, i.e., a capacitor with a close to 1 and a resistor with a close to 0.

The resistance R_1 calculated from the first semicircle, which we refer to as the SEI, changes significantly and non-monotonically: decreasing by the 500th cycle and increasing by the 2000th cycle within an order of magnitude. This may be due to the influence of two counteracting factors: (*a*) the expansion of SEI film surface area, which *decreases* R_1; and (*b*) SEI film thickness growth, which *increases* it.

The Warburg constant σ behaves similarly, decreasing for 1200 cycles, followed by an increase. Since the Warburg constant is proportional to the electrode surface area, its decrease indicates a growth of the electrode surface area during cycling, which is related to the material electrochemical milling and correlates with the change in R_1.

Table 2. Fitted parameters of FeOOH/PANI impedance spectra at the charged state.

Cycle No.	R_s, Ω	R_1, Ω	Q_1, F	a	σ, $\Omega{\cdot}s^{-0.5}$
5	23.4	164	1.8×10^{-5}	0.79	1200
60	13.8	93.8	2.6×10^{-5}	0.77	1130
150	29.9	45.0	2.3×10^{-5}	0.82	536
500	34.4	18.3	7.8×10^{-5}	0.80	90.1
1200	37.6	31.2	9.9×10^{-5}	0.74	52.3
2000	12.4	138	9.9×10^{-5}	0.58	126

The parameters from the fitting of the two semicircles using a series of parallel *R-CPE* elements for the discharge state (Table 3) show that there is a non-monotonic change in the Q_1 (SEI capacitance). Q_1 increases up to the 1200th cycle, followed by a decrease to the 2000th. In addition to the electrochemical milling, the SEI dielectric constant affects Q_1, the nature of which may change during the discharge since catalytic reduction of electrolyte components with the formation of a redox-active gel-like film is possible on iron particles [42,103]. The CPE exponent a_1 lies in the 0.75–0.88 range, showing that CPE_1 consistently exhibits capacitor-like behavior. This is also confirmed by the SEI capacitance increase in comparison to the charged state of the electrode. The SEI resistance R_1 behaves similarly to that of the charged state, the only difference being that its minimum is at the 150th cycle, followed by a gradual increase.

Just as in the case of the charged state of the cell, the electrolyte resistance R_s does not follow a trend and lies in the range from 12 Ω to 44 Ω.

The second semicircle refers to charge transfer resistance R_2 and the accompanying capacitance Q_2. The capacitance Q_2 behaves non-monotonically, and the parameter a_2 related to the matching of CPE behavior to either a resistor or capacitor also changes significantly within the experiment. First, Q_2 decreases up to the 150th cycle, then increases up to the 1200th one and remains at ca. 1×10^{-4} F till the end of cycling. This generally follows the dependence of the capacity on the cycle number shown in Figure 3b. This change in capacitance is due to electrochemical milling during cycling, which leads to a deterioration of the contact between the active material and the conductive additive. This results in a decrease in capacitance and an increase in resistance. Some FeOOH particles completely disconnect from the conductive matrix, leading to a Q_2 vs. cycle number dependence minimum. Despite this, the charge transfer resistance decreases up to the 500th cycle. Such behavior may be related to the phenomenon that occurred in particles that have maintained contact with the electrode conducting components: the interface between passivation film (SEI) and material, formed previously, cannot hinder Li^+ ion transfer, and hence resistance decreases [128]. As a result, the expected increase in resistance during the deterioration of the contact area with the conducting elements of the electrode is compensated by the facilitation of Li^+ ion transfer.

Table 3. Fitted parameters of FeOOH/PANI impedance spectra at discharged state.

Cycle	R_s, Ω	R_1, Ω	Q_1, F	a_1	R_2, Ω	Q_2, F	a_2	σ, Ω·s$^{-0.5}$
5	32	76	3.1×10^{-3}	0.78	180	1.1×10^{-4}	0.56	27
60	17	76	5.4×10^{-3}	0.75	100	8.4×10^{-5}	0.64	30
150	29	25	1.6×10^{-2}	0.83	37	6.3×10^{-5}	0.75	24
500	28	37	2.7×10^{-2}	0.88	17	9.4×10^{-5}	0.81	13
1200	44	49	2.4×10^{-2}	0.86	30	1.1×10^{-4}	0.73	9.8
2000	12	58	6.6×10^{-3}	0.78	36	1.1×10^{-4}	0.56	20

The Warburg constant (σ) for the discharged state demonstrates the same behavior as in the charged state, decreasing monotonically during the initial 1200 cycles, followed by an increase. Since the Warburg constant is inversely proportional to the electrode surface area [129], its decline indicates surface area growth related to the electrochemical milling of the material and correlates with the change in the SEI resistance.

The change in size induced by electrochemical milling can be calculated from PITT measurements using the Cottrell approach by applying a model for intercalation materials derived by Montella [126]. To do this, we performed chronoamperometric measurements at 1.5 V with a step of 0.01 V after the 5th, 50th, 150th, 500th, 1200th, and 2000th cycles. We chose this potential value since it reflects the process of lithium intercalation into FeOOH without the accompanying conversion reaction that directly leads to the milling (see Equation (4)). This means that regardless of particle size, the Li^+ diffusion coefficient will be the same, which allows the application of the Montella intercalation model for the size change calculations.

According to the Montella model, the maximum in $I\sqrt{t}$-lg$t$ dependency is proportional to the Li^+ diffusion coefficient D (cm^2·s^{-1}) and the characteristic diffusion length L (cm), which is equal to the particles◎radii in the case of spherical particles:

$$(I\sqrt{t})_{max} = \frac{\Delta Q\sqrt{D/\pi}}{L}, \tag{8}$$

where ΔQ (C) is the faradaic charge passed following a potential step, t (s) is the measurement time.

The existence of two maxima in $I\sqrt{t}$-lg$t$ dependency implies the appearance of new particles with another L value. The initial cycle shows only one peak, for which the L value is 300 nm, as seen in SEM (Figure 1a,b). Further cycling leads to the emergence of the second peak (Figures 8a and S5), with its intensity increasing and its position shifting towards higher $lg(t)$ values. Fitting $I\sqrt{t}$-lg$t$ dependencies yields $(I\sqrt{t})_{max}$ and ΔQ values for each particle size.

Equation (8) can be represented as follows:

$$(I\sqrt{t})_{max1} = \frac{\Delta Q_1\sqrt{D/\pi}}{L_1} \tag{9}$$

$$(I\sqrt{t})_{max2} = \frac{\Delta Q_2\sqrt{D/\pi}}{L_2} \tag{10}$$

Division of $(I\sqrt{t})_{max2}$ by $(I\sqrt{t})_{max1}$ yields the equation to calculate particles◎size:

$$L_2 = \frac{(I\sqrt{t})_{max1}}{(I\sqrt{t})_{max2}} \cdot \frac{\Delta Q_2}{\Delta Q_1} \cdot L_1 \tag{11}$$

From ΔQ_1 and ΔQ_2 we can calculate the mass fraction (W_2) of particles with the characteristic length L_2 depending on the cycle number:

$$W_2 = 100\% \cdot \frac{\Delta Q_2}{\Delta Q_1 + \Delta Q_2} \tag{12}$$

The calculated L_2 and W_2 values in Figure 8b show that the particles grow from 1.5 nm in the 5th cycle to 25 nm in the 150th one. The growth slows down during further cycling so that the size of the particles increases to 55 nm by the 2000th cycle. These results correlate with the drop and the following growth of capacity in FeOOH/PANI cycle life tests (Figure 3b).

These results also correlate with the Warburg constant value changes in EIS data. Again, assuming that particles are spherical—which is a reasonable outcome of the milling process—this formula provides the changes in a specific area of FeOOH/PANI during cycling [130]:

$$S = \frac{6}{\rho} \cdot \left(\frac{w_1}{d_1} + \frac{w_2}{d_2}\right), \quad (13)$$

where ρ is the FeOOH density, 4.0 g·cm^{-3}, w_1 is the mass ratio of the grains with the diameter d_1; w_2 is the mass ratio of the grains with the diameter d_1.

As seen in Figure 8c, the surface area of FeOOH/PANI sharply grows up to the 150th cycle, which is caused by an increase in the ratio of particles with a characteristic length L_2 under 10 nm. Then, the growth increases and reaches its maximum at 11.60 m^2·g^{-1} by the 2000th cycle. The dependencies of the Warburg constant and the surface area of the particles on the number of cycles are inversely proportional, thus confirming the validity of our assumptions that allowed us to calculate the characteristic length L_2 and the specific surface area S. These results also support that electrochemical milling of FeOOH/PANI particles occurs during cycling, reflected in the dependence of specific capacity on the cycle number (Figure 3b).

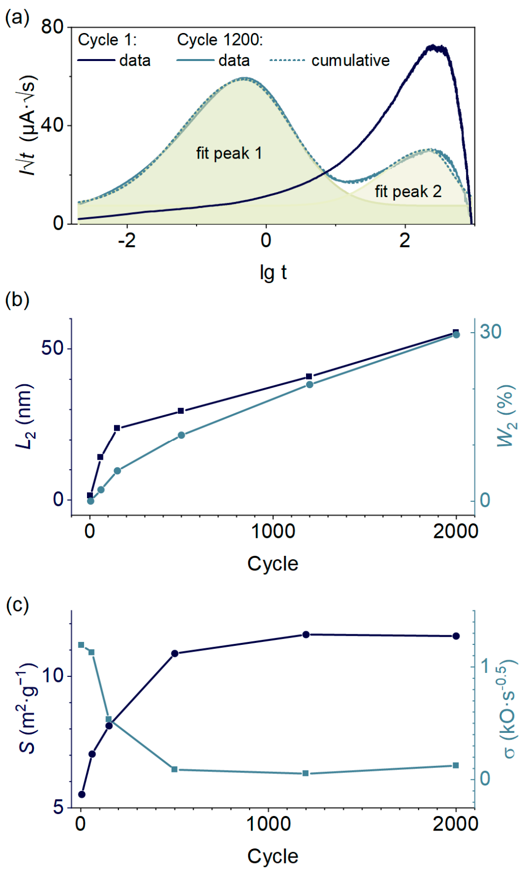

Figure 8. (**a**) Fitted Cottrell function plot for the current transient versus the decimal logarithm for 1st and 1200th cycles; (**b**) dependence of particle size L_2 and its mass content on the cycle number; (**c**) correlation between specific surface area from PITT and Warburg constant from EIS.

We conducted ex situ, FTIR, XPS, and SEM/EDX of FeOOH/PANI-based electrodes to investigate the structural changes and their effects on the charge storage mechanism in more detail. We recorded ATR FTIR spectra after cycling the FeOOH for a different number of cycles (Figure 9). Since the penetration depth of the ATR FTIR typically does not exceed 2 μm [131], the observed spectral response is mostly attributed to the products that form on the electrode surface. During the charge–discharge, rapid decrease in the bands at 3195 cm^{-1} and 3025 cm^{-1} was observed, indicating either dehydration of the material and/or the growth of the thick (>1 μm) SEI or gel–polymer coating on the material. An increase in the group of bands around (950–1100) cm^{-1} and 1480 cm^{-1}, corresponding to P-F and C-F stretching vibrations, indicates the formation of the electrolyte decomposition products. The combination of the bands at 1400 cm^{-1} and 845 cm^{-1} testifies to the presence of Li_2CO_3 or other inorganic carbonates.

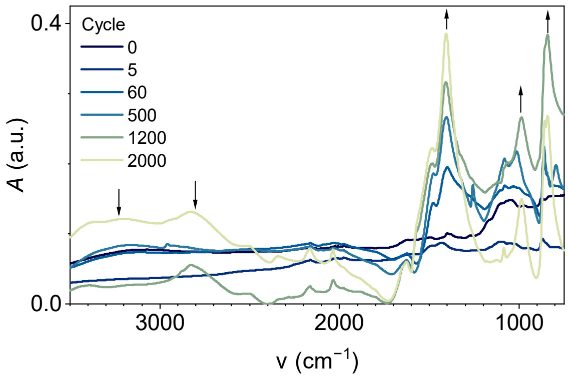

Figure 9. ATR-FTIR spectra of FeOOH/PANI electrodes after different number of recharging cycles.

The change in the FeOOH/PANI electrochemical behavior during long-term cycling may also be linked to the changes in SEI composition during this process, which we studied by XPS. The results are shown in Figures 10, S6 and S7, and Table 4. The table summarizes the position of the peaks and which compounds they belong to.

The spectra of the N 1s, Fe 2p, and O 1s (Figures S6 and 10) for the electrode prior to cycling (0 cycles) coincide with the pure FeOOH/PANI (Figure 2). The carbon spectrum shows bonds corresponding to carbon black, PANI, PVDF, and oxygen-containing groups on their surface. F 1s refers to PVDF. After 5 charge–discharge cycles, the surface composition of the electrode changes and continues changing throughout 2000 cycles. On the C 1s spectrum, the same peaks remain, which are related to carbon black and aliphatic chains. By cycle five, the intensity of the signals assigned to C in C-N-C, C-N$^+$-C, and -C=O groups decreases significantly, and C-F (PVDF) disappears completely. These signals might be overwhelmed by the newly emerged bands corresponding to inorganic and organic salts, i.e., the products of electrolyte decomposition: LiF and $Li_xPF_{y-1}O_{z+1}$ (not a product of complete decomposition of $LiPF_6$ [39]) in the F 1s spectrum, lithium carbonate and carboxylates in the C 1s, O 1s spectra, and the disappearance of positively charged nitrogen in the N 1s spectrum, which corresponds to the reduction of oxidized form of aniline, which is obtained during synthesis, to neutral, preserved throughout the cycling, as indicated by -N= and -NH- groups on the spectrum N 1s. Most likely, PANI changes from the protonated form to the lithiated one [56,132]. Despite the formation of electrolyte decomposition products on the electrode surface, the N 1s spectrum shape was preserved during cycling (Figure 10), although its intensity decreased compared to the zero cycle. This may be a consequence of electrode cracking during solvent drying and exposure of the innermost part of the electrode, which will be discussed below.

The C 1s spectrum shape remains stable between cycles 60 and 2000. At cycle 5, peaks of lithium carboxylates and carbonate appear, which significantly increase in intensity by cycle 60 (discharge capacity minimum) and persist until the end of cycling, which may indicate a diminished solvent reduction rate, which can be [40,41,133,134] represented by the following reactions:

$$C_2H_4OCO_2 + Li^+ + e^- \rightarrow C_2H_4OCO_2Li \quad (14)$$

$$2C_2H_4OCO_2 + 2Li^+ + 2e^- \rightarrow CH_2{-}CH_2 \uparrow + (CH_2OCO_2Li)_2 \quad (15)$$

$$C_2H_4OCO_2 + 2Li^+ + 2e^- \rightarrow CH_2{-}CH_2 \uparrow + Li_2CO_3 \quad (16)$$

$$(CH_3CH_2O)_2CO + 2Li^+ + 2e^- \rightarrow CH_3CH_2COOLi + CH_3CH_2OLi \quad (17)$$

Here, $C_2H_4OCO_2$ is ethylene carbonate, and $(CH_3CH_2O)_2CO$ is diethyl carbonate.

Also, by cycle 60, the LiF content increases significantly compared to $Li_xPF_{y-1}O_{z+1}$. Both are products of $LiPF_6$ decomposition in the presence of water or oxygen [39]. The reactions corresponding to the formation of these salts can be represented as follows [40,135]:

$$LiPF_6 \rightleftarrows LiF + PF_5 \quad (18)$$

$$PF_5 + H_2O \rightarrow POF_3 + 2HF \quad (19)$$

$$POF_3 + 2Li^+ + 2e^- \rightarrow Li_xPF_{y-1}O_{z-1} + LiF \quad (20)$$

$$Li_2CO_3 + LiPF_6 \rightarrow Li_xPF_{y-1}O_{z-1} + LiF + CO_2 \uparrow \quad (21)$$

$$2HF + Li_2CO_3 \rightarrow CO_2 \uparrow + 2LiF + H_2O \quad (22)$$

$$LiPF_6 + H_2O \rightarrow POF_3 + 2HF + LiF \quad (23)$$

The increased intensity of the $Li_xPF_{y-1}O_{z+1}$ peak in LiF after the 60th cycle indicates the continuing process of $LiPF_6$ decomposition. Obviously, during SEI formation up to cycle 60, the higher LiF content in SEI is explained by the substantial number of reactions for which it is a product (e.g., Equations (18)–(23)). Further cycling causes some of these reactions to slow down or stop. The availability of PANI makes it act as a conductive binder [136–139], into which iron oxide particles are redeposited. This leads to an increasing proportion of material involved in the storage capacity with the formation of products that stimulate $Li_xPF_{y-1}O_{z+1}$ generation.

An examination of the spectra of Li 1s + Fe 3p and Fe 2p (Figures S6 and S7) confirms the above-described behavior of the electrodes during cycling. In the initial sample (0 cycles), the Fe 2p spectrum completely coincides with the one in Figure 2, and only one peak related to Fe 3p is present in Li 1s + Fe 3p (Table 4). After the charge–discharge cycles, the intensity of the Fe 3p line decreases significantly, and a pronounced peak of Li 1s appears, referring to various salts: carbonates, fluoride, and carboxylates.

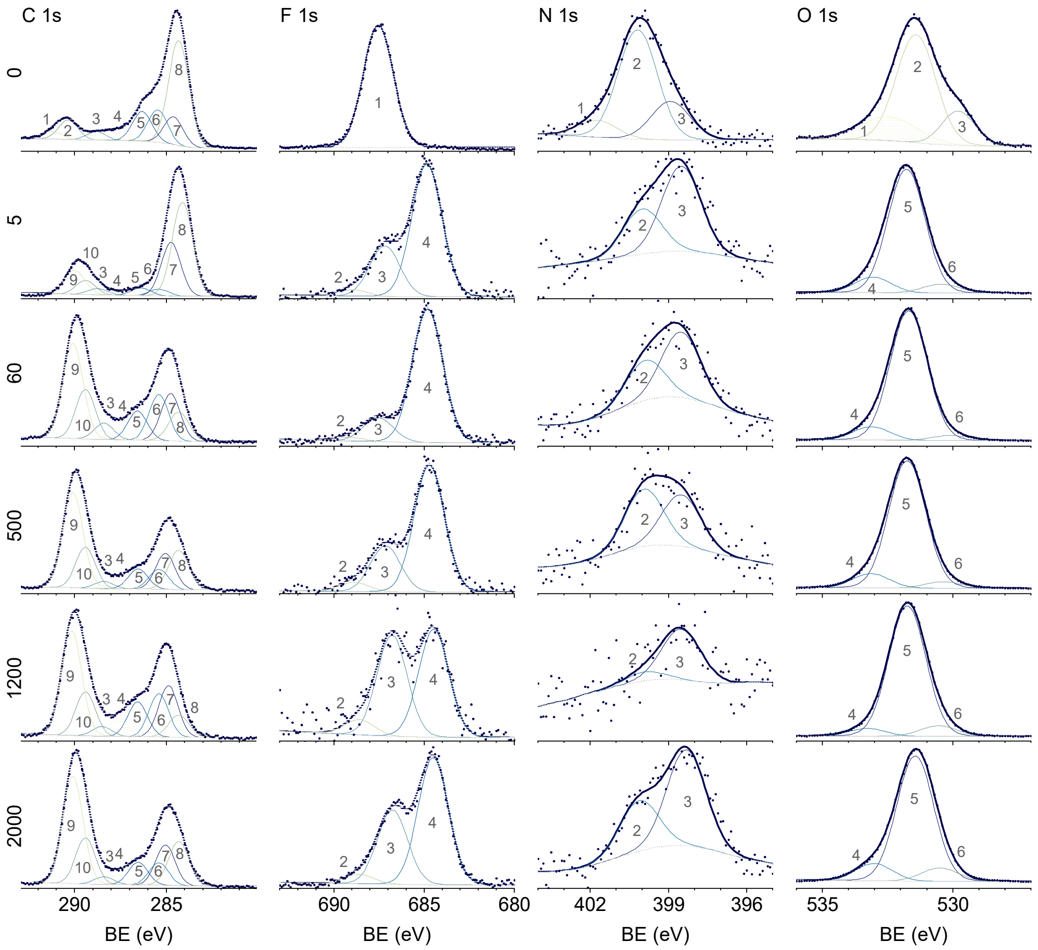

Figure 10. XPS spectra of C 1s, F 1s, N 1s, and O 1s for FeOOH/PANI electrode after cycling. The rows are for cycle numbers 0, 5, 60, 500, 1200, and 2000, and the columns are for the C, F, N, and O 1s bands. In each spectrum, dark blue dots are for experimental data, thick blue line is approximation curve, and dotted gray line is background curve. Fitted peaks assignment: in C 1s: **1**—C–F (C_nF_m) π-π*, **2**—C–F (PVDF), **3**—R–F (organoflourine), **4**—C=O, **5**—C–OH/C–N$^+$–C/CH_2–CH_2 (PVDF), **6**—C–N–C/C–O–C, **7**—C=C (sp^2), **8**—C–C (sp^3), **9**—Li_2CO_3, **10**—O=C–O; in F 1s: **1**—C–F (PVDF), **2**—LiF, **3**—$Li_xPO_{y-1}F_{z+1}$, **4**—C–F (C_nF_m); in N 1s: **1**—positively charged nitrogen (oxidized amine), **2**—benzenoid amine (–NH–), **3**—imine (–N=); in O 1s: **1**—SO_4^{2-}, **2**—Fe–OH, **3**—Fe=O, **4**—C–O–C/P–O–P, **5**—C=O/P=O/–OH, **6**—Fe in the oxide matrix.

Table 4. Peak positions of C 1s, F 1s, N 1s, O 1s, Li 1s in XPS data of cycled FeOOH/PANI electrodes.

Peak	Chem. Bond	Component	Sample BE after Cycling, eV						BE from References	
			0	5	60	500	1200	2000	BE, eV	Ref.
C 1s	C=C (sp^2)	carbon black	284.3	281.1	284.3	284.3	284.3	284.3	284.0–284.6	[33,140,141]
	H-C-C (sp^3)	aliphatic chain	284.6	284.6	284.7	285.0	284.9	285.0	284.6–286.0	[33,140,141]
	C-N-C/ C-O-C	PANI, ethers	285.4	285.4	285.4	285.4	285.4	285.4	285.3–286.0	[33,90,91,93]
	C-OH/ C-N$^+$-C/ CH_2-CH_2	alcohols, PANI, PVDF	286.3	286.4	286.5	286.5	286.5	286.5	286.3–286.7	[33,90,91,93]
	C=O	ketones, aldehydes	287.6	287.6	287.6	287.6	287.6	287.6	287.1–288.1	[33,140,141]
	R-F	organofluoric	288.8	288.8	288.4	288.4	288.5	288.4	287.7–290.2	[33,141,142]
	F-C-F	PVDF	290.3	-	-	-	-	-	-	[33]
	O-C(=O)-O	Li_2CO_3, semiorganic carbonates	-	290.1	290.1	290.1	290.1	290.1	289.6–290.1	[33,143,144]

F 1s	C-F	PVDF	687.5	-	-	-	-	-	687.3–687.9	[33,145,146]
	C-F	C_nF_m	-	689.0	689.2	688.9	688.7	688.6	688.4–690.0	[33,147–149]
	F-P-O	$Li_xPO_{y-1}F_{z+1}$	-	687.2	687.5	687.1	686.8	686.8	686.1–687.9	[33]
	Li-F	LiF	-	684.6	684.7	684.7	684.5	684.5	684.5–685.0	[33,150,151]
N 1s	N^+-H	oxidized amine,	401.7	-	-	-	-	-	401.1–401.7	[91,152,153]
	N-H	benzenoid amine	400.2	399.9	399.8	399.9	399.8	400.0	399.6–400.7	[91,92,153]
	-N=	imine	398.9	398.5	398.5	398.5	398.5	398.3	398.1–399.3	[91,92,152,154]
O 1s	Fe=O	FeOOH	529.9	-	-	-	-	-	530.0–530.5	[83,86,87]
	Fe-OH	FeOOH	531.4	-	-	-	-	-	531.2–531.6	[83,86,87]
	S=O, S-O^-	SO_4^{2-}	532.5	-	-	-	-	-	532.2–532.6	[88,89,147]
	Fe-O	Oxide matrix	-	530.5	530.2	530.3	530.5	530.5	530.0–530.5	[41,83,86,87]
	C=O, P=O, -OH	Alkoxide, carboxylate, esters, Li_2CO_3, $Li_xPO_{y-1}F_{z+1}$	-	531.8	531.7	531.8	531.7	531.5	531.2–532.0	[33,41,87]
	C-O-C, P-O-P	Organic carbonate, $Li_xPO_{y-1}F_{z+1}$, Li_xPO_y		533.1	533.1	533.1	533.2	533.1	531.1–533.8	[33,41]
Li 1s	Li-F Li-Oli P-Oli	LiF, carboxylates, Li_2CO_3, ROLi, $Li_xPO_{y-1}F_{z+1}$, Li_xPO_y	-	55.4	55.3	55.4	55.4	55.2	55.2–55.8	[33,41,155]
	Fe^{3+}	FeOOH	55.7	-	-	-	-	-	55.6–55.8	[156]
	Fe^{3+}	Oxide matrix	-	55.8	55.8	55.8	55.8	55.8	55.6–55.8	[156,157]
	Fe^{2+}	Oxide matrix	-	53.7	53.7	53.7	53.7	53.7	53.7–53.8	[156]

There are also weakly pronounced peaks of Fe^{2+} and Fe^{3+} corresponding to different states of iron in the oxide matrix. In the Fe 2p spectrum, two peaks are visually identified at 710.5 eV and 715.5 eV, which can be attributed to Fe^{2+} and Fe^{3+} in the Fe_3O_4 and FeO mixture [156]. By the 60th cycle, the iron lines disappear completely. This coincides with the cycle number with minimal specific capacity. Further cycling leads to an increase in both the capacity and the XPS lines◎intensities again, confirming the assumption of electrochemical milling of the material.

According to EDX analysis (Figure 11), the electrode surface changes significantly during long cycling, as does the elemental composition. Since the penetration depth of the energy dispersive spectroscopy typically does not exceed (0.02–1) μm [158], the elemental mapping results presented relate to a part of the electrode that is not immediately reflective of the entire electrode elemental contents. Specifically, for the results presented, the penetration depth did not exceed 500 nm. After 500 cycles, small spherical particles up to 200 nm appear on the surface; their number increases during cycling, and after 2000 cycles, they significantly cover the surface (Figure S8). Also, the figure shows that the electrode is abundantly covered by the electrolyte decomposition products, which causes it to crack into "islands" of different sizes. Electrode cracking after drying can be caused by a notable change in volume and an increase in internal stresses [42,159]. Among such decomposition products are various organic compounds that form a redox-active gel–polymer layer during the catalytic reduction of electrolyte on iron particles [160]. Microphotographs of the electrode confirm the formation of a decomposition product layer about 200 nm thick, covering the surface. Figure S8 also clearly shows the change in the shape of the FeOOH/PANI composite particles, which goes from urchin-like to rounded spherical with smooth edges by cycle 5, and to a complete inability to visually identify them by cycle 2000. Most likely, they are gradually pulverized and mixed with the electrolyte decomposition products.

The results of elemental mapping are shown in Figure 11. Oxygen content gradually increases along with the cycle number. The composition of the electrode for other elements changes non-monotonically: between cycles 60 and 1200, the sulfur signal disappears completely, which is most likely due to the sensitivity limit of the instrument; fluorine content decreases until cycle 60, then increases until cycle 500 and decreases again; phosphorus is not detected until cycle 60, decreasing gradually by cycle 1200 and then increasing by cycle 2000; iron content decreases gradually by cycle 60, then increases by cycle 500, and almost completely disappears by cycle 2000.

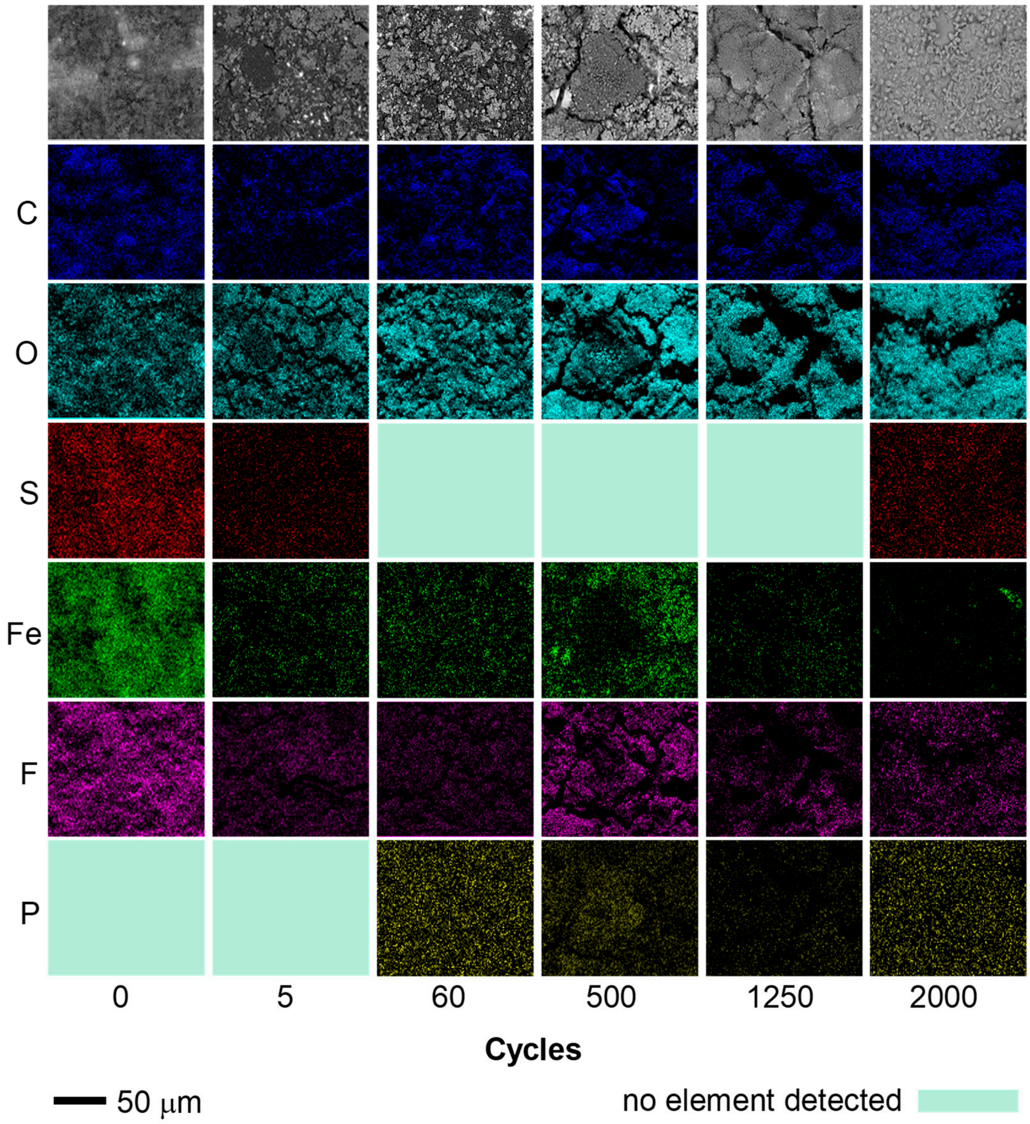

Figure 11. Element mapping for cycled electrodes obtained via EDX.

Thus, based on electrochemical (EIS) and physicochemical (ATR-FTIR, XPS, SEM/EDX) characterization methods, we can assume that the electrode composition constantly changes both internally and on the surface during cycling, i.e., the electrode is a dynamically evolving inhomogeneous system. At the same time, during cycling:

1. The porosity of the electrode increases, opening the access of the electrolyte to a more electroactive material.
2. The electrochemical milling of the electrode components first results in a sharp increase in the SEI amount, and, after SEI stabilizes, continued milling of FeOOH leads to an increase in capacity due to gradually improving contact of FeOOH with carbon black and PANI.

3. The electrode reaches a stable capacity after 1200 cycles, and the achieved capacity value corresponds to the original capacity of the electrode, as C-rate (Figure 3a) testing after the end of the long cycling shows.

Similar capacity behavior during cycling has been noted in several articles [102,161]. The duration of the capacity reaching a stable value also depends on the cycling current, similar to our previous report for FeOOH/Graphite [74] for 0.3 $A \cdot g^{-1}$ and 1.2 $A \cdot g^{-1}$. Therefore, it is particularly important to study the capacity "pit" formation as a function of the number of cycles influenced by the electrode transformation mode during the early cycles. Although this aspect is not covered in this study, it will be addressed in future research.

4. Conclusions

A simple one-step atmospheric plasma-assisted synthesis method was used to create an urchin-like FeOOH/PANI nanoparticle composite that was used in anode materials for LIBs for the first time. After 2000 cycles, FeOOH/PANI showed exceptional performance as anodes for Li-ion batteries in terms of their cycling behavior and capacity retention: 767 $mA \cdot h \cdot g^{-1}$ at 1.2 $A \cdot g^{-1}$, 1600 $mA \cdot h \cdot g^{-1}$ at 0.05 $A \cdot g^{-1}$, and 181 $mA \cdot h \cdot g^{-1}$ at 10 $A \cdot g^{-1}$. The capacity of the product exhibited two unusual trends during cycling at 1.2 $A \cdot g^{-1}$: a decrease in capacity to ca. 140 $mA \cdot h \cdot g^{-1}$ in the first (40–60) cycles, followed by a remarkable increase to 767 $mA \cdot h \cdot g^{-1}$ after 1200 cycles. The outstanding performance is attributed to the electrochemical milling effect, which results in a decrease in the nanoparticle size and the formation of a porous structure. This provides good structural stability and increases the contact between the electrode and electrolyte. As a result, the material fully regains its capacity after 1200 cycles and exhibits a value of 1600 $mA \cdot h \cdot g^{-1}$ at 0.05 $A \cdot g^{-1}$, which is equal to the first cycle's capacity. A comparison of full cells with the NMC532 cathode and FeOOH/PANI or graphite anodes revealed comparable specific energy characteristics: 224 $Wh \cdot kg^{-1}$ vs. 264 $Wh \cdot kg^{-1}$. This, along with the low cost, makes FeOOH/PANI anode materials appealing enough to replace existing graphite materials.

Supplementary Materials: The following supporting information can be downloaded at https://www.mdpi.com/article/10.3390/chemengineering8010024/s1. Figure S1: Synthesis setup diagram; Figure S2: Plots of particles' size distribution; Figure S3: XRD pattern of FeOOH/PANI powder; Figure S4: SEM images and EDX spectra of plasma solution synthesized FeOOH, PANI and FeOOH/PANI composite; electrical conductivity temperature dependence of FeOOH/PANI composite; and charge–discharge curve of the NMC532—Graphite full cell at a C/2 rate; Figure S5: Cottrell function plot for the current transient versus the decimal logarithm of time; Figure S6: XPS spectra of Fe 2p; Figure S7: XPS spectra of Li 1s + Fe 3p; Figure S8: Evolution of the electrode surface during 2000 cycles.

Author Contributions: Conceptualization, E.V.B.; investigation, E.V.B., K.A.K., O.V.G., M.A.K., and D.A.L.; formal analysis, E.V.B.; writing—original draft preparation, E.V.B., project administration, E.V.B.; supervision, E.V.B.; visualization, E.V.B. and A.I.V.; writing–review and editing, A.I.V., K.A.K., D.A.L., and O.V.L.; resources, M.A.K.; validation, O.V.L.; funding acquisition, O.V.L. All authors have read and agreed to the published version of the manuscript.

Funding: The work was supported by St Petersburg University, project 101746712 "Practice-oriented approach to the development of batteries based on organic materials".

Data Availability Statement: The data generated in this study may be provided by the corresponding authors upon reasonable request.

Acknowledgments: We thank the following resource centers of the Research Park of St. Petersburg State University. The Resource Center "Physical methods of surface investigation" for the XPS. The Resource Center "Nanotechnology" for the SEM/EDX and ATR-FTIR studies. The Research Centre for X-ray Diffraction Studies for XRD measurements.

Conflicts of Interest: The authors declare no conflict of interest.

References

1. Zubi, G.; Dufo-López, R.; Carvalho, M.; Pasaoglu, G. The Lithium-Ion Battery: State of the Art and Future Perspectives. *Renew. Sustain. Energy Rev.* **2018**, *89*, 292–308. https://doi.org/10.1016/j.rser.2018.03.002.
2. Manthiram, A. An Outlook on Lithium Ion Battery Technology. *ACS Cent. Sci.* **2017**, *3*, 1063–1069. https://doi.org/10.1021/acscentsci.7b00288.
3. Armand, M.; Axmann, P.; Bresser, D.; Copley, M.; Edström, K.; Ekberg, C.; Guyomard, D.; Lestriez, B.; Novák, P.; Petranikova, M.; et al. Lithium-Ion Batteries—Current State of the Art and Anticipated Developments. *J. Power Sources* **2020**, *479*, 228708. https://doi.org/10.1016/j.jpowsour.2020.228708.
4. Cheng, H.; Shapter, J.G.; Li, Y.; Gao, G. Recent Progress of Advanced Anode Materials of Lithium-Ion Batteries. *J. Energy Chem.* **2021**, *57*, 451–468. https://doi.org/10.1016/j.jechem.2020.08.056.
5. Roy, P.; Srivastava, S.K. Nanostructured Anode Materials for Lithium Ion Batteries. *J. Mater. Chem. A* **2015**, *3*, 2454–2484. https://doi.org/10.1039/c4ta04980b.
6. Chen, R.; Nolan, A.M.; Lu, J.; Wang, J.; Yu, X.; Mo, Y.; Chen, L.; Huang, X.; Li, H. The Thermal Stability of Lithium Solid Electrolytes with Metallic Lithium. *Joule* **2020**, *4*, 812–821. https://doi.org/10.1016/j.joule.2020.03.012.
7. Pu, K.-C.; Zhang, X.; Qu, X.-L.; Hu, J.-J.; Li, H.-W.; Gao, M.-X.; Pan, H.-G.; Liu, Y.-F. Recently Developed Strategies to Restrain Dendrite Growth of Li Metal Anodes for Rechargeable Batteries. *Rare Met.* **2020**, *39*, 616–635. https://doi.org/10.1007/s12598-020-01432-2.
8. Wu, Y.-P.; Rahm, E.; Holze, R. Carbon Anode Materials for Lithium Ion Batteries. *J. Power Sources* **2003**, *114*, 228–236. https://doi.org/10.1016/S0378-7753(02)00596-7.
9. Andre, D.; Hain, H.; Lamp, P.; Maglia, F.; Stiaszny, B. Future High-Energy Density Anode Materials from an Automotive Application Perspective. *J. Mater. Chem. A* **2017**, *5*, 17174–17198. https://doi.org/10.1039/C7TA03108D.
10. Poizot, P.; Laruelle, S.; Grugeon, S.; Dupont, L.; Tarascon, J.-M. Nano-Sized Transition-Metal Oxides as Negative-Electrode Materials for Lithium-Ion Batteries. *Nature* **2000**, *407*, 496–499. https://doi.org/10.1038/35035045.
11. Yoon, T.; Kim, J.; Kim, J.; Lee, J. Electrostatic Self-Assembly of Fe_3O_4 Nanoparticles on Graphene Oxides for High Capacity Lithium-Ion Battery Anodes. *Energies* **2013**, *6*, 4830–4840. https://doi.org/10.3390/en6094830.
12. Qin, D.; Yan, P.; Li, G.; Wang, Y.; An, Y.; Xing, J. Synthesis of Hierarchical CoO Nano/Microstructures as Anode Materials for Lithium-Ion Batteries. *J. Nanomater.* **2014**, *2014*, 489862. https://doi.org/10.1155/2014/489862.
13. Subalakshmi, P.; Sivashanmugam, A. Nano Co_3O_4 as Anode Material for Li–Ion and Na-Ion Batteries: An Insight into Surface Morphology. *ChemistrySelect* **2018**, *3*, 5040–5049. https://doi.org/10.1002/slct.201702197.
14. Bhatt, M.D.; Lee, J.Y. High Capacity Conversion Anodes in Li-Ion Batteries: A Review. *Int. J. Hydrogen Energy* **2019**, *44*, 10852–10905. https://doi.org/10.1016/j.ijhydene.2019.02.015.
15. Debart, A.; Dupont, L.; Poizot, P.; Leriche, J.B.; Tarascon, J.M. A Transmission Electron Microscopy Study of the Reactivity Mechanism of Tailor-Made CuO Particles toward Lithium. *J. Electrochem. Soc.* **2001**, *148*, A1266. https://doi.org/10.1149/1.1409971.
16. Hong, I.; Angelucci, M.; Verrelli, R.; Betti, M.G.; Panero, S.; Croce, F.; Mariani, C.; Scrosati, B.; Hassoun, J. Electrochemical Characteristics of Iron Oxide Nanowires during Lithium-Promoted Conversion Reaction. *J. Power Sources* **2014**, *256*, 133–136. https://doi.org/10.1016/j.jpowsour.2014.01.052.
17. Nanda, J.; Zhou, H.; Martha, S.K.; Li, J.; Dai, S.; Pannala, S.; Wang, J.; Braun, P.V.; Dudney, N.J.; Adcock, J. Molecular and Electrode Arcitectures for Multivalent Conversion Electrodes. *ECS Meet. Abstr.* **2014**, *MA2014-02*, 483. https://doi.org/10.1149/ma2014-02/6/483.
18. Imtiaz, M.; Chen, Z.; Zhu, C.; Pan, H.; Zada, I.; Li, Y.; Bokhari, S.W.; Luan, R.Y.; Nigar, S.; Zhu, S. In Situ Growth of β-FeOOH on Hierarchically Porous Carbon as Anodes for High-Performance Lithium-Ion Batteries. *Electrochim. Acta* **2018**, *283*, 401–409. https://doi.org/10.1016/j.electacta.2018.06.140.
19. Carbonari, G.; Maroni, F.; Gabrielli, S.; Staffolani, A.; Tossici, R.; Palmieri, A.; Nobili, F. Synthesis and Characterization of Vanillin-Templated Fe2O3 Nanoparticles as a Sustainable Anode Material for Li-Ion Batteries. *ChemElectroChem* **2019**, *6*, 1915–1920. https://doi.org/10.1002/celc.201900189.
20. Salunkhe, T.T.; Varma, R.S.; Kadam, A.N.; Lee, S.-W.; Lee, Y.-C.; Hur, J.; Kim, I.T. Scraps to Superior Anodes for Li-Ion Batteries: Sustainable and Scalable Upgrading of Waste Rust. *J. Hazard. Mater.* **2021**, *410*, 124571. https://doi.org/10.1016/j.jhazmat.2020.124571.
21. Wang, X.; Chen, X.; Gao, L.; Zheng, H.; Ji, M.; Tang, C.; Shen, T.; Zhang, Z. Synthesis of β-FeOOH and α-Fe_2O_3 Nanorods and Electrochemical Properties of β-FeOOH. *J. Mater. Chem.* **2004**, *14*, 905–907. https://doi.org/10.1039/B310722A.
22. Lou, X.; Wu, X.; Zhang, Y. Goethite Nanorods as Anode Electrode Materials for Rechargeable Li-Ion Batteries. *Electrochem. Commun.* **2009**, *11*, 1696–1699. https://doi.org/10.1016/j.elecom.2009.06.032.
23. Peng, S.; Yu, L.; Sun, M.; Cheng, G.; Lin, T.; Mo, Y.; Li, Z. Bunched Akaganeite Nanorod Arrays: Preparation and High-Performance for Flexible Lithium-Ion Batteries. *J. Power Sources* **2015**, *296*, 237–244. https://doi.org/10.1016/j.jpowsour.2015.07.023.
24. Zhai, Y.; Xu, L.; Qian, Y. Ce-Doped α-FeOOH Nanorods as High-Performance Anode Material for Energy Storage. *J. Power Sources* **2016**, *327*, 423–431. https://doi.org/10.1016/j.jpowsour.2016.07.051.
25. Liang, B.; Zhu, S.; Wang, J.; Liang, X.; Huang, H.; Huang, D.; Zhou, W.; Xu, S.; Guo, J. Silicon-Doped FeOOH Nanorods@graphene Sheets as High-Capacity and Durable Anodes for Lithium-Ion Batteries. *Appl. Surf. Sci.* **2021**, *550*, 149330. https://doi.org/10.1016/j.apsusc.2021.149330.

26. Qi, H.; Huang, J.; Tang, L.; Ma, M.; Deng, W.; Zhang, C. Confined Pulverization Promoting Durable Pseudocapacitance for FeOOH@PEDOT Anode in Li-Ion Battery. *J. Electroanal. Chem.* **2021**, *882*, 115005. https://doi.org/10.1016/j.jelechem.2021.115005.
27. Jin, X.; Li, Y.; Jin, T.; Jiang, J.; Zhu, Q.; Yao, J. Facile and Efficient Synthesis of Binary FeOOH/Fe_2O_3 Composite as a High-Performance Anode Material for Lithium-Ion Batteries. *J. Alloys Compd.* **2022**, *896*, 163026. https://doi.org/10.1016/j.jallcom.2021.163026.
28. Amine, K.; Yasuda, H.; Yamachi, M. β-FeOOH, a New Positive Electrode Material for Lithium Secondary Batteries. *J. Power Sources* **1999**, *81*, 221–223. https://doi.org/10.1016/S0378-7753(99)00138-X.
29. Tabuchi, T.; Katayama, Y.; Nukuda, T.; Ogumi, Z. β-FeOOH Thin Film as Positive Electrode for Lithium-Ion Cells. *J. Power Sources* **2009**, *191*, 640–643. https://doi.org/10.1016/j.jpowsour.2009.02.022.
30. Mukai, K.; Yamada, I. ϵ-FeOOH: A Novel Negative Electrode Material for Li-and Na-Ion Batteries. *ACS Omega* **2020**, *5*, 10115–10122. https://doi.org/10.1021/acsomega.0c00728.
31. Yu, L.; Xi, S.; Wei, C.; Zhang, W.; Du, Y.; Yan, Q.; Xu, Z. Superior Lithium Storage Properties of β-FeOOH. *Adv. Energy Mater.* **2015**, *5*, 1401517. https://doi.org/10.1002/aenm.201401517.
32. Tabuchi, T.; Katayama, Y.; Nukuda, T.; Ogumi, Z. Surface Reaction of β-FeOOH Film Negative Electrode for Lithium-Ion Cells. *J. Power Sources* **2009**, *191*, 636–639. https://doi.org/10.1016/j.jpowsour.2009.02.021.
33. Schulz, N.; Hausbrand, R.; Wittich, C.; Dimesso, L.; Jaegermann, W. XPS-Surface Analysis of SEI Layers on Li-Ion Cathodes: Part II. SEI-Composition and Formation inside Composite Electrodes. *J. Electrochem. Soc.* **2018**, *165*, A833–A846. https://doi.org/10.1149/2.0881803jes.
34. Peled, E. The Electrochemical Behavior of Alkali and Alkaline Earth Metals in Nonaqueous Battery Systems—The Solid Electrolyte Interphase Model. *J. Electrochem. Soc.* **1979**, *126*, 2047. https://doi.org/10.1149/1.2128859.
35. Verma, P.; Maire, P.; Novák, P. A Review of the Features and Analyses of the Solid Electrolyte Interphase in Li-Ion Batteries. *Electrochim. Acta* **2010**, *55*, 6332–6341. https://doi.org/10.1016/j.electacta.2010.05.072.
36. Nie, M.; Chalasani, D.; Abraham, D.P.; Chen, Y.; Bose, A.; Lucht, B.L. Lithium Ion Battery Graphite Solid Electrolyte Interphase Revealed by Microscopy and Spectroscopy. *J. Phys. Chem. C* **2013**, *117*, 1257–1267. https://doi.org/10.1021/jp3118055.
37. Nie, M.; Lucht, B.L. Role of Lithium Salt on Solid Electrolyte Interface (SEI) Formation and Structure in Lithium Ion Batteries. *J. Electrochem. Soc.* **2014**, *161*, A1001. https://doi.org/10.1149/2.054406jes.
38. Heiskanen, S.K.; Kim, J.; Lucht, B.L. Generation and Evolution of the Solid Electrolyte Interphase of Lithium-Ion Batteries. *Joule* **2019**, *3*, 2322–2333. https://doi.org/10.1016/j.joule.2019.08.018.
39. Parimalam, B.S.; Lucht, B.L. Reduction Reactions of Electrolyte Salts for Lithium Ion Batteries: LiPF6, LiBF4, LiDFOB, LiBOB, and LiTFSI. *J. Electrochem. Soc.* **2018**, *165*, A251–A255. https://doi.org/10.1149/2.0901802jes.
40. An, S.J.; Li, J.; Daniel, C.; Mohanty, D.; Nagpure, S.; Wood, D.L. The State of Understanding of the Lithium-Ion-Battery Graphite Solid Electrolyte Interphase (SEI) and Its Relationship to Formation Cycling. *Carbon N. Y.* **2016**, *105*, 52–76. https://doi.org/10.1016/j.carbon.2016.04.008.
41. Bock, D.C.; Waller, G.H.; Mansour, A.N.; Marschilok, A.C.; Takeuchi, K.J.; Takeuchi, E.S. Investigation of Solid Electrolyte Interphase Layer Formation and Electrochemical Reversibility of Magnetite, Fe_3O_4, Electrodes: A Combined X-ray Absorption Spectroscopy and X-ray Photoelectron Spectroscopy Study. *J. Phys. Chem. C* **2018**, *122*, 14257–14271. https://doi.org/10.1021/acs.jpcc.8b01970.
42. Laruelle, S.; Grugeon, S.; Poizot, P.; Dollé, M.; Dupont, L.; Tarascon, J.-M. On the Origin of the Extra Electrochemical Capacity Displayed by MO/Li Cells at Low Potential. *J. Electrochem. Soc.* **2002**, *149*, A627. https://doi.org/10.1149/1.1467947.
43. Tian, B.; Światowska, J.; Maurice, V.; Zanna, S.; Seyeux, A.; Klein, L.H.; Marcus, P. Combined Surface and Electrochemical Study of the Lithiation/Delithiation Mechanism of the Iron Oxide Thin-Film Anode for Lithium-Ion Batteries. *J. Phys. Chem. C* **2013**, *117*, 21651–21661. https://doi.org/10.1021/jp4064438.
44. Rezvani, S.J.; Nobili, F.; Gunnella, R.; Ali, M.; Tossici, R.; Passerini, S.; Di Cicco, A. SEI Dynamics in Metal Oxide Conversion Electrodes of Li-Ion Batteries. *J. Phys. Chem. C* **2017**, *121*, 26379–26388. https://doi.org/10.1021/acs.jpcc.7b08259.
45. Kraytsberg, A.; Ein-Eli, Y. A Critical Review-Promises and Barriers of Conversion Electrodes for Li-Ion Batteries. *J. Solid State Electrochem.* **2017**, *21*, 1907–1923. https://doi.org/10.1007/s10008-017-3580-9.
46. Zhao, H.; Song, Z.; Gao, H.; Li, B.; Hu, T.; Liu, F.; Sohn, H.Y. The Structure-Directing Role of Graphene in Composites with Porous FeOOH Nanorods for Li Ion Batteries. *RSC Adv.* **2020**, *10*, 41403–41409. https://doi.org/10.1039/d0ra07125k.
47. Chen, Y.X.; He, L.H.; Shang, P.J.; Tang, Q.L.; Liu, Z.Q.; Liu, H.; Zhou, L.P. Micro-Sized and Nano-Sized Fe_3O_4 Particles as Anode Materials for Lithium-Ion Batteries. *J. Mater. Sci. Technol.* **2011**, *27*, 41–45. https://doi.org/10.1016/S1005-0302(11)60023-6.
48. Zhong, G.; Qu, K.; Ren, C.; Su, Y.; Fu, B.; Zi, M.; Dai, L.; Xiao, Q.; Xu, J.; Zhong, X. Epitaxial Array of Fe_3O_4 Nanodots for High Rate High Capacity Conversion Type Lithium Ion Batteries Electrode with Long Cycling Life. *Nano Energy* **2020**, *74*, 104876. https://doi.org/10.1016/j.nanoen.2020.104876.
49. Yu, L.; Wei, C.; Yan, Q.; Xu, Z.J. Controlled Synthesis of High-Performance β-FeOOH Anodes for Lithium-Ion Batteries and Their Size Effects. *Nano Energy* **2015**, *13*, 397–404. https://doi.org/10.1016/j.nanoen.2015.03.003.
50. Zhu, S.; Liang, B.; Mou, X.; Liang, X.; Huang, H.; Huang, D.; Zhou, W.; Xu, S.; Guo, J. In-Situ Synthesis of F-Doped FeOOH Nanorods on Graphene as Anode Materials for High Lithium Storage. *J. Alloys Compd.* **2022**, *905*, 164142. https://doi.org/10.1016/j.jallcom.2022.164142.
51. Wang, C.; Yang, X.; Zheng, M.; Xu, Y. Synthesis of β-FeOOH Nanorods Adhered to Pine-Biomass Carbon as a Low-Cost Anode Material for Li-Ion Batteries. *J. Alloys Compd.* **2019**, *794*, 569–575. https://doi.org/10.1016/j.jallcom.2019.04.074.

52. Raccichini, R.; Varzi, A.; Wei, D.; Passerini, S. Critical Insight into the Relentless Progression toward Graphene and Graphene-containing Materials for Lithium-ion Battery Anodes. *Adv. Mater.* **2017**, *29*, 1603421. https://doi.org/10.1002/adma.201603421.
53. Bryan, A.M.; Santino, L.M.; Lu, Y.; Acharya, S.; D'Arcy, J.M. Conducting Polymers for Pseudocapacitive Energy Storage. *Chem. Mater.* **2016**, *28*, 5989–5998. https://doi.org/10.1021/acs.chemmater.6b01762.
54. Kim, J.; Lee, J.; You, J.; Park, M.-S.; Al Hossain, M.S.; Yamauchi, Y.; Kim, J.H. Conductive Polymers for Next-Generation Energy Storage Systems: Recent Progress and New Functions. *Mater. Horizons* **2016**, *3*, 517–535. https://doi.org/10.1039/C6MH00165C.
55. Tajik, S.; Beitollahi, H.; Nejad, F.G.; Shoaie, I.S.; Khalilzadeh, M.A.; Asl, M.S.; Van Le, Q.; Zhang, K.; Jang, H.W.; Shokouhimehr, M. Recent Developments in Conducting Polymers: Applications for Electrochemistry. *RSC Adv.* **2020**, *10*, 37834–37856. https://doi.org/10.1039/D0RA06160C.
56. Eliseeva, S.N.; Kamenskii, M.A.; Tolstopyatova, E.G.; Kondratiev, V.V. Effect of Combined Conductive Polymer Binder on the Electrochemical Performance of Electrode Materials for Lithium-Ion Batteries. *Energies* **2020**, *13*, 2163. https://doi.org/10.3390/en13092163.
57. Sharma, R.; Nihal; Sharma, M.; Goswamy, J.K. $LiMn_2O_4$-rGO/PANI Nanocomposite as a Cathode Material for Li-Ion Batteries. *J. Electrochem. Soc.* **2022**, *169*, 083505. https://doi.org/10.1149/1945-7111/ac86f9.
58. Kiran, L.; Aydınol, M.K.; Ahmad, A.; Shah, S.S.; Bahtiyar, D.; Shahzad, M.I.; Eldin, S.M.; Bahajjaj, A.A.A. Flowers Like α-MoO_3/CNTs/PANI Nanocomposites as Anode Materials for High-Performance Lithium Storage. *Molecules* **2023**, *28*, 3319. https://doi.org/10.3390/molecules28083319.
59. Patil, M.; Jang, H.; Han, S.-H.; Gattu, K.P.; Tonpe, D.A.; Kutwade, V.V.; Sharma, R. Electrochemical Performance of Low-Cost PANI-Anchored CuS Electrode for Lithium-Ion Batteries. *Appl. Phys. A* **2023**, *129*, 142. https://doi.org/10.1007/s00339-023-06417-3.
60. Zhang, M.; Han, D.; Lu, P. PEDOT Encapsulated β-FeOOH Nanorods: Synthesis, Characterization and Application for Sodium-Ion Batteries. *Electrochim. Acta* **2017**, *238*, 330–336. https://doi.org/10.1016/j.electacta.2017.04.040.
61. Gong, X.; Li, S.; Lee, P.S. A Fiber Asymmetric Supercapacitor Based on FeOOH/PPy on Carbon Fibers as an Anode Electrode with High Volumetric Energy Density for Wearable Applications. *Nanoscale* **2017**, *9*, 10794–10801. https://doi.org/10.1039/C7NR02896B.
62. Wei, G.; Du, K.; Zhao, X.; Li, C.; Li, J.; Ren, K.; Huang, Y.; Wang, H.; Yao, S.; An, C. Integrated FeOOH Nanospindles with Conductive Polymer Layer for High-Performance Supercapacitors. *J. Alloys Compd.* **2017**, *728*, 631–639. https://doi.org/10.1016/j.jallcom.2017.09.002.
63. Sakaebe, H.; Higuchi, S.; Kanamura, K.; Fujimoto, H.; Takehara, Z. Discharge and Charge Characteristics of Amorphous FeOOH Including Aniline (Aan-FeOOH): Influence of Preparation Conditions on Discharge and Charge Characteristics. *J. Electrochem. Soc.* **1995**, *142*, 360. https://doi.org/10.1149/1.2044009.
64. Ma, H.; Zheng, Y.; Xian, J.; Feng, Z.; Li, Z.; Cui, F. A Light-Enhanced α-FeOOH Nanowires/Polyaniline Anode for Improved Electricity Generation Performance in Microbial Fuel Cells. *Chemosphere* **2022**, *296*, 133994. https://doi.org/10.1016/j.chemosphere.2022.133994.
65. Xiong, H.; Zhang, B.; Cui, C.; Xu, Y. Polyaniline/FeOOH Composite for Removal of Acid Orange II from Aqueous Solutions. *Mater. Chem. Phys.* **2022**, *278*, 125701. https://doi.org/10.1016/j.matchemphys.2022.125701.
66. Javed, M.S.; Khan, A.J.; Hanif, M.; Nazir, M.T.; Hussain, S.; Saleem, M.; Raza, R.; Yun, S.; Liu, Z. Engineering the Performance of Negative Electrode for Supercapacitor by Polyaniline Coated Fe_3O_4 Nanoparticles Enables High Stability up to 25,000 Cycles. *Int. J. Hydrogen Energy* **2021**, *46*, 9976–9987. https://doi.org/10.1016/j.ijhydene.2020.04.173.
67. Wang, S.; Hu, L.; Hu, Y.; Jiao, S. Conductive Polyaniline Capped Fe_2O_3 Composite Anode for High Rate Lithium Ion Batteries. *Mater. Chem. Phys.* **2014**, *146*, 289–294. https://doi.org/10.1016/j.matchemphys.2014.03.025.
68. Ma, R.; Wang, M.; Dam, D.T.; Yoon, Y.; Chen, Y.; Lee, J. Polyaniline-Coated Hollow Fe_2O_3 Nanoellipsoids as an Anode Material for High-Performance Lithium-Ion Batteries. *ChemElectroChem* **2015**, *2*, 503–507. https://doi.org/10.1002/celc.201402402.
69. Wang, Q.; Wang, X.; Chai, Z.; Hu, W. Low-Temperature Plasma Synthesis of Carbon Nanotubes and Graphene Based Materials and Their Fuel Cell Applications. *Chem. Soc. Rev.* **2013**, *42*, 8821–8834. https://doi.org/10.1039/c3cs60205b.
70. Dou, S.; Tao, L.; Wang, R.; El Hankari, S.; Chen, R.; Wang, S. Plasma-assisted Synthesis and Surface Modification of Electrode Materials for Renewable Energy. *Adv. Mater.* **2018**, *30*, 1705850. https://doi.org/10.1002/adma.201705850.
71. Iqbal, T.; Aziz, A.; Khan, M.A.; Andleeb, S.; Mahmood, H.; Khan, A.A.; Khan, R.; Shafique, M. Surfactant Assisted Synthesis of ZnO Nanostructures Using Atmospheric Pressure Microplasma Electrochemical Process with Antibacterial Applications. *Mater. Sci. Eng. B* **2018**, *228*, 153–159. https://doi.org/10.1016/j.mseb.2017.11.027.
72. Oehrlein, G.S.; Hamaguchi, S. Foundations of Low-Temperature Plasma Enhanced Materials Synthesis and Etching. *Plasma Sources Sci. Technol.* **2018**, *27*, 023001. https://doi.org/10.1088/1361-6595/aaa86c.
73. Tiya-Djowe, A.; Laminsi, S.; Noupeyi, G.L.; Gaigneaux, E.M. Non-Thermal Plasma Synthesis of Sea-Urchin like α-FeOOH for the Catalytic Oxidation of Orange II in Aqueous Solution. *Appl. Catal. B Environ.* **2015**, *176–177*, 99–106. https://doi.org/10.1016/j.apcatb.2015.03.053.
74. Beletskii, E.V.; Kamenskii, M.A.; Alekseeva, E.V.; Volkov, A.I.; Lukyanov, D.A.; Anishchenko, D.V.; Radomtseu, A.O.; Reveguk, A.A.; Glumov, O.V.; Levin, O.V. One-Step Atmospheric Plasma-Assisted Synthesis of FeOOH and FeOOH/Graphite High Performance Anode Materials for Lithium-Ion Batteries. *Appl. Surf. Sci.* **2022**, *597*, 153698. https://doi.org/10.1016/j.apsusc.2022.153698.

75. Michel, M.; Bour, J.; Petersen, J.; Arnoult, C.; Ettingshausen, F.; Roth, C.; Ruch, D. Atmospheric Plasma Deposition: A New Pathway in the Design of Conducting Polymer-Based Anodes for Hydrogen Fuel Cells. *Fuel Cells* **2010**, *10*, 932–937. https://doi.org/10.1002/fuce.201000050.
76. Park, C.-S.; Kim, D.H.; Shin, B.J.; Tae, H.-S. Synthesis and Characterization of Nanofibrous Polyaniline Thin Film Prepared by Novel Atmospheric Pressure Plasma Polymerization Technique. *Materials* **2016**, *9*, 39. https://doi.org/10.3390/ma9010039.
77. Iqbal, S. In-Situ Iodine Doping Characteristics of Conductive Polyaniline Film Polymerized by Low-Voltage-Driven Atmospheric Pressure Plasma. *Polymers* **2021**, *13*, 418. https://doi.org/10.3390/polym13030418.
78. Jeong, J.; Choi, B.G.; Lee, S.C.; Lee, K.G.; Chang, S.; Han, Y.; Lee, Y.B.; Lee, H.U.; Kwon, S.; Lee, G.; et al. Hierarchical Hollow Spheres of Fe_2O_3 @Polyaniline for Lithium Ion Battery Anodes. *Adv. Mater.* **2013**, *25*, 6250–6255. https://doi.org/10.1002/adma.201302710.
79. Wang, X.; Liu, Y.; Han, H.; Zhao, Y.; Ma, W.; Sun, H. Polyaniline Coated Fe_3O_4 Hollow Nanospheres as Anode Materials for Lithium Ion Batteries. *Sustain. Energy Fuels* **2017**, *1*, 915–922. https://doi.org/10.1039/c7se00139h.
80. Zhang, Z.; Bi, X.; Li, X.; Zhao, Q.; Chen, H. Schwertmannite: Occurrence, Properties, Synthesis and Application in Environmental Remediation. *RSC Adv.* **2018**, *8*, 33583–33599. https://doi.org/10.1039/C8RA06025H.
81. Jönsson, J.; Persson, P.; Sjöberg, S.; Lövgren, L. Schwertmannite Precipitated from Acid Mine Drainage: Phase Transformation, Sulphate Release and Surface Properties. *Appl. Geochem.* **2005**, *20*, 179–191. https://doi.org/10.1016/j.apgeochem.2004.04.008.
82. Gupta, R.P.; Sen, S.K. Calculation of Multiplet Structure of Core p -Vacancy Levels. II. *Phys. Rev. B* **1975**, *12*, 15–19. https://doi.org/10.1103/PhysRevB.12.15.
83. McIntyre, N.S.; Zetaruk, D.G. X-ray Photoelectron Spectroscopic Studies of Iron Oxides. *Anal. Chem.* **1977**, *49*, 1521–1529. https://doi.org/10.1021/ac50019a016.
84. Descostes, M.; Mercier, F.; Thromat, N.; Beaucaire, C.; Gautier-Soyer, M. Use of XPS in the Determination of Chemical Environment and Oxidation State of Iron and Sulfur Samples: Constitution of a Data Basis in Binding Energies for Fe and S Reference Compounds and Applications to the Evidence of Surface Species of an Oxidized Py. *Appl. Surf. Sci.* **2000**, *165*, 288–302. https://doi.org/10.1016/S0169-4332(00)00443-8.
85. Grosvenor, A.P.; Kobe, B.A.; Biesinger, M.; Mcintyre, N. Investigation of Multiplet Splitting of Fe 2p XPS Spectra and Bonding in Iron Compounds. *Surf. Interface Anal.* **2004**, *36*, 1564–1574. https://doi.org/10.1002/sia.1984.
86. Welsh, I.D.; Sherwood, P.M.A. Photoemission and Electronic Structure of FeOOH: Distinguishing between Oxide and Oxyhydroxide. *Phys. Rev. B* **1989**, *40*, 6386–6392. https://doi.org/10.1103/PhysRevB.40.6386.
87. Chemelewski, W.D.; Lee, H.-C.; Lin, J.-F.; Bard, A.J.; Mullins, C.B. Amorphous FeOOH Oxygen Evolution Reaction Catalyst for Photoelectrochemical Water Splitting. *J. Am. Chem. Soc.* **2014**, *136*, 2843–2850. https://doi.org/10.1021/ja411835a.
88. Lindberg, B.J.; Hamrin, K.; Johansson, G.; Gelius, U.; Fahlman, A.; Nordling, C.; Siegbahn, K. Molecular Spectroscopy by Means of ESCA II. Sulfur Compounds. Correlation of Electron Binding Energy with Structure. *Phys. Scr.* **1970**, *1*, 286–298. https://doi.org/10.1088/0031-8949/1/5-6/020.
89. Naumkin, A.V.; Kraut-Vass, A.; Gaarenstroom, S.W.; Powell, C.J. NIST X-ray Photoelectron Spectroscopy Database. Available online: https://dx.doi.org/10.18434/T4T88K (accessed on 13 September 2023).
90. Snauwaert, P.; Lazzaroni, R.; Riga, J.; Verbist, J.J. Electronic Structure of Polyaniline and Substituted Derivatives. *Synth. Met.* **1987**, *18*, 335–340. https://doi.org/10.1016/0379-6779(87)90901-5.
91. Golczak, S.; Kanciurzewska, A.; Fahlman, M.; Langer, K.; Langer, J.J. Comparative XPS Surface Study of Polyaniline Thin Films. *Solid State Ionics* **2008**, *179*, 2234–2239. https://doi.org/10.1016/j.ssi.2008.08.004.
92. Waghmode, B.J.; Patil, S.H.; Jahagirdar, M.M.; Patil, V.S.; Waichal, R.P.; Malkhede, D.D.; Sathaye, S.D.; Patil, K.R. Studies on Morphology of Polyaniline Films Formed at Liquid–Liquid and Solid–Liquid Interfaces at 25 and 5 °C, Respectively, and Effect of Doping. *Colloid Polym. Sci.* **2014**, *292*, 1079–1089. https://doi.org/10.1007/s00396-013-3150-3.
93. Ciriello, R.; Carbone, M.E.; Coviello, D.; Guerrieri, A.; Salvi, A.M. Improved Stability of Thin Insulating Poly(o-Aminophenol) Films in Aqueous Solutions through an Efficient Strategy for Electrosynthesis under Neutral PH Conditions: Electrochemical and XPS Investigation. *J. Electroanal. Chem.* **2020**, *867*, 114183. https://doi.org/10.1016/j.jelechem.2020.114183.
94. Wang, R.; Yoshino, T. Electrical Conductivity of Diaspore, δ-AlOOH and ϵ-FeOOH. *Am. Mineral.* **2021**, *106*, 774–781. https://doi.org/10.2138/am-2021-7605.
95. Focke, W.W.; Wnek, G.E.; Wei, Y. Influence of Oxidation State, PH, and Counterion on the Conductivity of Polyaniline. *J. Phys. Chem.* **1987**, *91*, 5813–5818. https://doi.org/10.1021/j100306a059.
96. Chulkin, P.; Łapkowski, M. An Insight into Ionic Conductivity of Polyaniline Thin Films. *Materials* **2020**, *13*, 2877. https://doi.org/10.3390/ma13122877.
97. Kaneko, K.; Inouye, K. Electrical Conductivity Changes in α-FeOOH and β-FeOOH upon Surface Dehydration. *Bull. Chem. Soc. Jpn.* **1976**, *49*, 3689–3690. https://doi.org/10.1246/bcsj.49.3689.
98. Bhadra, J.; Al-Thani, N.J.; Madi, N.K.; Al-Maadeed, M.A. Effects of Aniline Concentrations on the Electrical and Mechanical Properties of Polyaniline Polyvinyl Alcohol Blends. *Arab. J. Chem.* **2017**, *10*, 664–672. https://doi.org/10.1016/j.arabjc.2015.04.017.
99. Bednarczyk, K.; Matysiak, W.; Tański, T.; Janeczek, H.; Schab-Balcerzak, E.; Libera, M. Effect of Polyaniline Content and Protonating Dopants on Electroconductive Composites. *Sci. Rep.* **2021**, *11*, 7487. https://doi.org/10.1038/s41598-021-86950-4.
100. Yuqin, C.; Hong, L.; Lie, W.; Tianhong, L. Irreversible Capacity Loss of Graphite Electrode in Lithium-Ion Batteries. *J. Power Sources* **1997**, *68*, 187–190. https://doi.org/10.1016/S0378-7753(96)02549-9.

101. Shim, J.; Striebel, K.A. Effect of Electrode Density on Cycle Performance and Irreversible Capacity Loss for Natural Graphite Anode in Lithium-Ion Batteries. *J. Power Sources* **2003**, *119–121*, 934–937. https://doi.org/10.1016/S0378-7753(03)00235-0.
102. Hassan, M.F.; Guo, Z.; Chen, Z.; Liu, H. α-Fe_2O_3 as an Anode Material with Capacity Rise and High Rate Capability for Lithium-Ion Batteries. *Mater. Res. Bull.* **2011**, *46*, 858–864. https://doi.org/10.1016/j.materresbull.2011.02.011.
103. Kim, H.; Choi, W.; Yoon, J.; Um, J.H.; Lee, W.; Kim, J.; Cabana, J.; Yoon, W.S. Exploring Anomalous Charge Storage in Anode Materials for Next-Generation Li Rechargeable Batteries. *Chem. Rev.* **2020**, *120*, 6934–6976. https://doi.org/10.1021/acs.chemrev.9b00618.
104. Chen, C.; Ding, N.; Wang, L.; Yu, Y.; Lieberwirth, I. Some New Facts on Electrochemical Reaction Mechanism for Transition Metal Oxide Electrodes. *J. Power Sources* **2009**, *189*, 552–556. https://doi.org/10.1016/j.jpowsour.2008.10.052.
105. Zou, M.; Wen, W.; Li, J.; Lin, Y.; Lai, H.; Huang, Z. Nano-Crystalline FeOOH Mixed with SWNT Matrix as a Superior Anode Material for Lithium Batteries. *J. Energy Chem.* **2014**, *23*, 513–518. https://doi.org/10.1016/S2095-4956(14)60179-0.
106. Zhai, Y.; Ma, X.; Mao, H.; Shao, W.; Xu, L.; He, Y.; Qian, Y. Mn-Doped α-FeOOH Nanorods and α-Fe_2O_3 Mesoporous Nanorods: Facile Synthesis and Applications as High Performance Anodes for LIBs. *Adv. Electron. Mater.* **2015**, *1*, 1400057. https://doi.org/10.1002/aelm.201400057.
107. Luo, L.; Wu, J.; Xu, J.; Dravid, V.P. Atomic Resolution Study of Reversible Conversion Reaction in Metal Oxide Electrodes for Lithium-Ion Battery. *ACS Nano* **2014**, *8*, 11560–11566. https://doi.org/10.1021/nn504806h.
108. Brezesinski, T.; Wang, J.; Tolbert, S.H.; Dunn, B. Ordered Mesoporous α-MoO_3 with Iso-Oriented Nanocrystalline Walls for Thin-Film Pseudocapacitors. *Nat. Mater.* **2010**, *9*, 146–151. https://doi.org/10.1038/nmat2612.
109. Chao, D.; Zhu, C.; Yang, P.; Xia, X.; Liu, J.; Wang, J.; Fan, X.; Savilov, S.V.; Lin, J.; Fan, H.J.; et al. Array of Nanosheets Render Ultrafast and High-Capacity Na-Ion Storage by Tunable Pseudocapacitance. *Nat. Commun.* **2016**, *7*, 12122. https://doi.org/10.1038/ncomms12122.
110. Forghani, M.; Donne, S.W. Method Comparison for Deconvoluting Capacitive and Pseudo-Capacitive Contributions to Electrochemical Capacitor Electrode Behavior. *J. Electrochem. Soc.* **2018**, *165*, A664–A673. https://doi.org/10.1149/2.0931803jes.
111. Kang, N.; Park, J.H.; Choi, J.; Jin, J.; Chun, J.; Jung, I.G.; Jeong, J.; Park, J.-G.; Lee, S.M.; Kim, H.J.; et al. Nanoparticulate Iron Oxide Tubes from Microporous Organic Nanotubes as Stable Anode Materials for Lithium Ion Batteries. *Angew. Chemie* **2012**, *124*, 6730–6734. https://doi.org/10.1002/ange.201202244.
112. Zhang, X.; Du, Y. Gelatin Assisted Wet Chemistry Synthesis of High Quality β-FeOOH Nanorods Anchored on Graphene Nanosheets with Superior Lithium-Ion Battery Application. *RSC Adv.* **2016**, *6*, 17504–17509. https://doi.org/10.1039/c5ra28170a.
113. Chen, X.; Zeng, Y.; Chen, Z.; Wang, S.; Xin, C.; Wang, L.; Shi, C.; Lu, L.; Zhang, C. Synthesis and Electrochemical Property of FeOOH/Graphene Oxide Composites. *Front. Chem.* **2020**, *8*, 328. https://doi.org/10.3389/fchem.2020.00328.
114. Wei, S.; Di Lecce, D.; Hassoun, J. A High-Voltage, Multi-Metal $LiNi_{0.35}Cu_{0.1}Mn_{1.45}Fe_{0.1}O_4$ Spinel Cathode for Lithium Batteries. *J. Electrochem. Soc.* **2021**, *168*, 30537. https://doi.org/10.1149/1945-7111/abed22.
115. Pan, T.; Alvarado, J.; Zhu, J.; Yue, Y.; Xin, H.L.; Nordlund, D.; Lin, F.; Doeff, M.M. Structural Degradation of Layered Cathode Materials in Lithium-Ion Batteries Induced by Ball Milling. *J. Electrochem. Soc.* **2019**, *166*, A1964. https://doi.org/10.1149/2.0091910jes.
116. Beletskii, E.V.; Volkov, A.I.; Alekseeva, E. V.; Anishchenko, D. V.; Konev, A.S.; Levin, O. V Potential-Controlled Switchable-Resistance Polymer Layer for Enhanced Safety of Lithium-Ion Batteries with NMC-Type Cathodes. *ACS Appl. Energy Mater.* **2023**, *166*, A1964–A1971. https://doi.org/10.1021/acsaem.3c02145.
117. Wang, Q.; Sarkar, A.; Li, Z.; Lu, Y.; Velasco, L.; Bhattacharya, S.S.; Brezesinski, T.; Hahn, H.; Breitung, B. High Entropy Oxides as Anode Material for Li-Ion Battery Applications: A Practical Approach. *Electrochem. Commun.* **2019**, *100*, 121–125. https://doi.org/10.1016/j.elecom.2019.02.001.
118. He, Y.; Xu, G.; Wang, C.; Xu, L.; Zhang, K. Horsetail-Derived Si@N-Doped Carbon as Low-Cost and Long Cycle Life Anode for Li-Ion Half/Full Cells. *Electrochim. Acta* **2018**, *264*, 173–182. https://doi.org/10.1016/j.electacta.2018.01.088.
119. Yao, Z.; Xia, X.; Zhang, Y.; Xie, D.; Ai, C.; Lin, S.; Wang, Y.; Deng, S.; Shen, S.; Wang, X.; et al. Superior High-Rate Lithium-Ion Storage on $Ti_2Nb_{10}O_{29}$ Arrays via Synergistic TiC/C Skeleton and N-Doped Carbon Shell. *Nano Energy* **2018**, *54*, 304–312. https://doi.org/10.1016/j.nanoen.2018.10.024.
120. Xu, T.; Wang, Q.; Zhang, J.; Xie, X.; Xia, B. Green Synthesis of Dual Carbon Conductive Network-Encapsulated Hollow SiOx Spheres for Superior Lithium-Ion Batteries. *ACS Appl. Mater. Interfaces* **2019**, *11*, 19959–19967. https://doi.org/10.1021/acsami.9b03070.
121. Deng, T.; Fan, X.; Cao, L.; Chen, J.; Hou, S.; Ji, X.; Chen, L.; Li, S.; Zhou, X.; Hu, E.; et al. Designing In-Situ-Formed Interphases Enables Highly Reversible Cobalt-Free $LiNiO_2$ Cathode for Li-Ion and Li-Metal Batteries. *Joule* **2019**, *3*, 2550–2564. https://doi.org/10.1016/j.joule.2019.08.004.
122. Zhu, Z.; Wang, H.; Li, Y.; Gao, R.; Xiao, X.; Yu, Q.; Wang, C.; Waluyo, I.; Ding, J.; Hunt, A.; et al. A Surface Se-Substituted $LiCo[O_{2-\delta}Se_\delta]$ Cathode with Ultrastable High-Voltage Cycling in Pouch Full-Cells. *Adv. Mater.* **2020**, *32*, 2005182. https://doi.org/10.1002/adma.202005182.
123. Shen, Y.; Qian, J.; Yang, H.; Zhong, F.; Ai, X. Chemically Prelithiated Hard-Carbon Anode for High Power and High Capacity Li-Ion Batteries. *Small* **2020**, *16*, 1907602. https://doi.org/10.1002/smll.201907602.
124. Yan, M.-Y.; Li, G.; Zhang, J.; Tian, Y.-F.; Yin, Y.-X.; Zhang, C.-J.; Jiang, K.-C.; Xu, Q.; Li, H.-L.; Guo, Y.-G. Enabling SiOx/C Anode with High Initial Coulombic Efficiency through a Chemical Pre-Lithiation Strategy for High-Energy-Density Lithium-Ion Batteries. *ACS Appl. Mater. Interfaces* **2020**, *12*, 27202–27209. https://doi.org/10.1021/acsami.0c05153.

125. Meng, T.; Li, B.; Wang, Q.; Hao, J.; Huang, B.; Gu, F.L.; Xu, H.; Liu, P.; Tong, Y. Large-Scale Electric-Field Confined Silicon with Optimized Charge-Transfer Kinetics and Structural Stability for High-Rate Lithium-Ion Batteries. *ACS Nano* **2020**, *14*, 7066–7076. https://doi.org/10.1021/acsnano.0c01796.
126. Montella, C. Discussion of the Potential Step Method for the Determination of the Diffusion Coefficients of Guest Species in Host Materials: Part I. Influence of Charge Transfer Kinetics and Ohmic Potential Drop. *J. Electroanal. Chem.* **2002**, *518*, 61–83. https://doi.org/10.1016/S0022-0728(01)00691-X.
127. Jiang, Y.; Jiang, Z.-J.; Yang, L.; Cheng, S.; Liu, M. A High-Performance Anode for Lithium Ion Batteries: Fe_3O_4 Microspheres Encapsulated in Hollow Graphene Shells. *J. Mater. Chem. A* **2015**, *3*, 11847–11856. https://doi.org/10.1039/C5TA01848J.
128. Kang, Y.-M.; Song, M.-S.; Kim, J.-H.; Kim, H.-S.; Park, M.-S.; Lee, J.-Y.; Liu, H.K.; Dou, S.X. A Study on the Charge–Discharge Mechanism of Co_3O_4 as an Anode for the Li Ion Secondary Battery. *Electrochim. Acta* **2005**, *50*, 3667–3673. https://doi.org/10.1016/j.electacta.2005.01.012.
129. Pyun, S.-I.; Bae, J.-S. The Ac Impedance Study of Electrochemical Lithium Intercalation into Porous Vanadium Oxide Electrode. *Electrochim. Acta* **1996**, *41*, 919–925. https://doi.org/10.1016/0013-4686(95)00386-X.
130. Ghasemi, Y.; Emborg, M.; Cwirzen, A. Estimation of Specific Surface Area of Particles Based on Size Distribution Curve. *Mag. Concr. Res.* **2018**, *70*, 533–540. https://doi.org/10.1680/jmacr.17.00045.
131. Mirabella, F.M. *Internal Reflection Spectroscopy: Theory and Applications*; CRC Press: Boca Raton, FL, USA, 1992; Volume 15. ISBN 0824787307.
132. Feng, M.; Tian, J.; Xie, H.; Kang, Y.; Shan, Z. Nano-Silicon/Polyaniline Composites with an Enhanced Reversible Capacity as Anode Materials for Lithium Ion Batteries. *J. Solid State Electrochem.* **2015**, *19*, 1773–1782. https://doi.org/10.1007/s10008-015-2807-x.
133. Zhuang, G.; Chen, Y.; Ross, P.N. The Reaction of Lithium with Dimethyl Carbonate and Diethyl Carbonate in Ultrahigh Vacuum Studied by X-ray Photoemission Spectroscopy. *Langmuir* **1999**, *15*, 1470–1479. https://doi.org/10.1021/la980454y.
134. Wang, A.; Kadam, S.; Li, H.; Shi, S.; Qi, Y. Review on Modeling of the Anode Solid Electrolyte Interphase (SEI) for Lithium-Ion Batteries. *npj Comput. Mater.* **2018**, *4*, 15. https://doi.org/10.1038/s41524-018-0064-0.
135. Markevich, E.; Salitra, G.; Hartmann, P.; Kulisch, J.; Aurbach, D.; Park, K.-J.; Yoon, C.; Sun, Y.-K. New Insights Related to Rechargeable Lithium Batteries: Li Metal Anodes, Ni Rich $LiNi_xCo_yMn_zO_2$ Cathodes and Beyond Them. *J. Electrochem. Soc.* **2019**, *166*, A5265–A5274. https://doi.org/10.1149/2.0261903jes.
136. Lee, K.; Lim, S.; Tron, A.; Mun, J.; Kim, Y.-J.; Yim, T.; Kim, T.-H. Polymeric Binder Based on PAA and Conductive PANI for High Performance Silicon-Based Anodes. *RSC Adv.* **2016**, *6*, 101622–101625. https://doi.org/10.1039/C6RA23805J.
137. Lin, H.-Y.; Li, C.-H.; Wang, D.-Y.; Chen, C.-C. Chemical Doping of a Core–Shell Silicon Nanoparticles@polyaniline Nanocomposite for the Performance Enhancement of a Lithium Ion Battery Anode. *Nanoscale* **2016**, *8*, 1280–1287. https://doi.org/10.1039/C5NR07152F.
138. Wang, X.; Zhang, Y.; Shi, Y.; Zeng, X.; Tang, R.; Wei, L. Conducting Polyaniline/Poly (Acrylic Acid)/Phytic Acid Multifunctional Binders for Si Anodes in Lithium Ion Batteries. *Ionics* **2019**, *25*, 5323–5331. https://doi.org/10.1007/s11581-019-03122-1.
139. Rajeev, K.K.; Kim, E.; Nam, J.; Lee, S.; Mun, J.; Kim, T.-H. Chitosan-Grafted-Polyaniline Copolymer as an Electrically Conductive and Mechanically Stable Binder for High-Performance Si Anodes in Li-Ion Batteries. *Electrochim. Acta* **2020**, *333*, 135532. https://doi.org/10.1016/j.electacta.2019.135532.
140. Barron, A.R.; Pavan M.V.R.. *Physical Methods in Chemistry and Nano Science*; Rice University: Houston, TX, USA, 2015.
141. Morgan, D.J. Comments on the XPS Analysis of Carbon Materials. *C* **2021**, *7*, 51. https://doi.org/10.3390/c7030051.
142. Sun, W.; Wang, L.; Yang, Z.; Zhu, T.; Wu, T.; Dong, C.; Liu, G. Tuning the Oxidation Degree of Graphite toward Highly Thermally Conductive Graphite/Epoxy Composites. *Chem. Mater.* **2018**, *30*, 7473–7483. https://doi.org/10.1021/acs.chemmater.8b01902.
143. Lee, J.; Choi, W. Surface Modification of Over-Lithiated Layered Oxides with PEDOT:PSS Conducting Polymer in Lithium-Ion Batteries. *J. Electrochem. Soc.* **2015**, *162*, A743–A748. https://doi.org/10.1149/2.0801504jes.
144. Maximov, M.; Nazarov, D.; Rumyantsev, A.; Koshtyal, Y.; Ezhov, I.; Mitrofanov, I.; Kim, A.; Medvedev, O.; Popovich, A. Atomic Layer Deposition of Lithium-Nickel-Silicon Oxide Cathode Material for Thin-Film Lithium-Ion Batteries. *Energies* **2020**, *13*, 2345. https://doi.org/10.3390/en13092345.
145. Dedryvère, R.; Maccario, M.; Croguennec, L.; Le Cras, F.; Delmas, C.; Gonbeau, D. X-Ray Photoelectron Spectroscopy Investigations of Carbon-Coated $LixFePO_4$ Materials. *Chem. Mater.* **2008**, *20*, 7164–7170. https://doi.org/10.1021/cm801995p.
146. Beletskii, E.V.; Fedorova, A.A.; Lukyanov, D.A.; Kalnin, A.Y.; Ershov, V.A.; Danilov, S.E.; Spiridonova, D.V.; Alekseeva, E.V.; Levin, O.V. Switchable Resistance Conducting-Polymer Layer for Li-Ion Battery Overcharge Protection. *J. Power Sources* **2021**, *490*, 229548. https://doi.org/10.1016/j.jpowsour.2021.229548.
147. Bennettand, H.; Ouver, G.J. High Resolution XPS of Organic Polymers: The Scienta ESCA300 Database (Beamson, G.; Briggs, D.). *J. Chem. Educ.* **1993**, *70*, A25. https://doi.org/10.1021/ed070pA25.5.
148. Kassis, C.M.; Steehler, J.K.; Linton, R.W. Characterization of 1,1-Dihydroperfluorooctyl Acrylate (PFOA) by XPS. *Surf. Sci. Spectra* **1994**, *3*, 299–306. https://doi.org/10.1116/1.1247742.
149. Hernández, M.P.; Navarro-Marín, G.; Estévez-Hernández, O.; Farías Sánchez, M.H. Angle-Resolved X-ray Photoelectron Spectroscopy Study of the Thiourea Derivative Adsorption on Au(111) from Ethanolic Solution. *Rev. Cuba. Fis.* **2017**, *34*, 108–111.

150. Huang, T.; Zheng, x.; Fang, G.; Pan, Y.; Wang, W.; Wu, M. A Novel Electrolyte Additive for Improving the Interfacial Stability of $LiMn_2O_4$ Cathode Lithium-Ion Batteries at Elevated Temperature. *RSC Adv.* **2018**, *8*, 38831–38835. https://doi.org/10.1039/c8ra08355j.
151. Moretti, A.; Carvalho, D.; Ehteshami-Flammer, N.; Paillard, E.; Porcher, W.; Brun-Buisson, D.; Ducros, J.-B.; Meatza, I.; Eguía-Barrio, A.; Trad, K.; et al. A Post-Mortem Study of Stacked 16 Ah Graphite//$LiFePO_4$ Pouch Cells Cycled at 5 °C. *Batteries* **2019**, *5*, 45. https://doi.org/10.3390/batteries5020045.
152. Kang, E.T.; Neoh, K.G.; Khor, S.H.; Tan, K.L.; Tan, B.T.G. X.p.s. Studies of Charge Transfer Interactions in Some Polyaniline Complexes. *Polymer* **1990**, *31*, 202–207. https://doi.org/10.1016/0032-3861(90)90106-9.
153. Quílez-Bermejo, J.; Morallón, E.; Cazorla-Amorós, D. Polyaniline-Derived N-Doped Ordered Mesoporous Carbon Thin Films: Efficient Catalysts towards Oxygen Reduction Reaction. *Polymers* **2020**, *12*, 2382. https://doi.org/10.3390/polym12102382.
154. Kumar, S.N.; Gaillard, F.; Bouyssoux, G.; Sartre, A. High-Resolution XPS Studies of Electrochemically Synthesized Conducting Polyaniline Films. *Synth. Met.* **1990**, *36*, 111–127. https://doi.org/10.1016/0379-6779(90)90240-L.
155. Wijaya, O.; Hartmann, P.; Younesi, R.; Markovits, I.I.E.; Rinaldi, A.; Janek, J.; Yazami, R. A Gamma Fluorinated Ether as an Additive for Enhanced Oxygen Activity in Li–O_2 Batteries. *J. Mater. Chem. A* **2015**, *3*, 19061–19067. https://doi.org/10.1039/C5TA03439F.
156. Yamashita, T.; Hayes, P. Analysis of XPS Spectra of Fe^{2+} and Fe^{3+} Ions in Oxide Materials. *Appl. Surf. Sci.* **2008**, *254*, 2441–2449. https://doi.org/10.1016/j.apsusc.2007.09.063.
157. Bagus, P.S.; Ilton, E.S.; Nelin, C.J. The Interpretation of XPS Spectra: Insights into Materials Properties. *Surf. Sci. Rep.* **2013**, *68*, 273–304. https://doi.org/10.1016/j.surfrep.2013.03.001.
158. Gibson, L.T. Archaeometry and antique analysis|Metallic and Ceramic Objects. In *Encyclopedia of Analytical Science*, 2nd ed.; Worsfold, P., Townshend, A., Poole, C.E., Eds.; Elsevier: Oxford, UK, 2005; pp. 117–123. ISBN 978-0-12-369397-6.
159. Tomar, B.S.; Shahin, A.; Tirumkudulu, M.S. Cracking in Drying Films of Polymer Solutions. *Soft Matter* **2020**, *16*, 3476–3484. https://doi.org/10.1039/C9SM02294E.
160. Zeng, Z.; Zhao, H.; Lv, P.; Zhang, Z.; Wang, J.; Xia, Q. Electrochemical Properties of Iron Oxides/Carbon Nanotubes as Anode Material for Lithium Ion Batteries. *J. Power Sources* **2015**, *274*, 1091–1099. https://doi.org/10.1016/j.jpowsour.2014.10.181.
161. Wen, J.-W.; Zhang, D.-W.; Zang, Y.; Sun, X.; Cheng, B.; Ding, C.-X.; Yu, Y.; Chen, C.-H. Li and Na Storage Behavior of Bowl-like Hollow Co_3O_4 Microspheres as an Anode Material for Lithium-Ion and Sodium-Ion Batteries. *Electrochim. Acta* **2014**, *132*, 193–199. https://doi.org/10.1016/j.electacta.2014.03.139.